Politecnico di Torino

Politecnico di Torino

Master Degree in Environmental and Land Engineering

Academic Year 2024/2025

March 2026

Spatial analysis of Integrated Water Vapor using Low-Cost GNSS Network

Supervisor:
Prof. Paolo Dabove

Cosupervisor:
Milad Bagheri

Candidate:
Lucrezia Bucci

Abstract

In recent years, Global Navigation Satellite Systems (GNSS) have been increasingly used in meteorology and climatology, replacing traditional techniques for measuring atmospheric parameters. Despite the extensive global network of permanent GNSS stations around the world, current spatial resolutions are not sufficient to provide high spatial resolution data, which is necessary for climate models and weather prediction. The Low-cost GNSS network of receivers offers a cheaper, simplified, and more accessible solution. This study assesses the accuracy of Integrated Water Vapor (IWV) estimations from the Centipede low-cost network. The analysis focuses on a dataset of 13 stations located in South-Eastern France during a one-week summer period, from 19 July 2025 to 25 July 2025.

GNSS observations provide measurements of the Zenith Tropospheric Delay (ZTD), which represents the delay experienced by signals while they propagate through the troposphere. ZTD can be separated into Zenith Hydrostatic Delay and Zenith Wet Delay, the latter being directly correlated to IWV. ZTD values are obtained through the Canadian Spatial Reference System Precise Point Positioning service, and IWV values are subsequently retrieved from ZWD. To address the spatial gap between stations, interpolation with External Drift Kriging is implemented.

Model validation is conducted through both cross-validation and independent comparison with data from the EUREF Permanent Network. The results show a good accuracy, with a root mean square error of 1.2 mm. This outcome not only proves that low-cost GNSS networks can provide high-quality atmospheric data, but also validates the robustness of the interpolation model in predicting missing water vapor measurements.

These findings indicate that low-cost GNSS networks can significantly enhance the spatial density of tropospheric water vapor observations. Their reduced operational costs also facilitate atmospheric monitoring in resource-limited regions, where traditional high-cost infrastructures may not be feasible. Given the increasing risk posed by climate change, such infrastructures are essential to improve the quality of climate models and weather forecasts.

Acknowledgments

I am sincerely grateful to my supervisor, Professor Paolo Dabove, for his expert guidance and for providing me with the independence to develop my own ideas within this study. His support has been fundamental to the completion of this thesis.
My thanks also go to Milad Bagheri, for his constant availability, kindness, and support during every step of this project. Collaborating with him has been profoundly inspiring and stimulating.

Contents

List of Figures

List of Tables

Chapter 1

Introduction

1.1 General introduction to Global Navigation Satellite System (GNSS)

Global Navigation Satellite System (GNSS) is any space-based system that supports users in delivering global Positioning, Navigation and Timing services (PNT) (EU Agency for the Space Programme, 2025). The main Global Navigation Satellite Systems are the US's GPS (Global Positioning System), the Russian GLONASS, the EU's Galileo and the Chinese BeiDou Satellite Navigation System (BDS). Beyond the major global constellations, a number of regional and augmentation systems enhance positioning performance and reliability, such as Japan's Quasi-Zenith Satellite System (QZSS), India's Regional Navigation Satellite System (IRNSS), and several Satellite-Based Augmentation Systems (SBAS) implemented worldwide.

The ongoing evolution of satellite navigation technologies, together with improvements in ground observation networks, has substantially expanded the range of potential GNSS applications across multiple domains (Jin et al., 2021). GNSS is currently used mostly for navigation purposes across a wide range of sectors, including transportation, telecommunications, land surveying, law enforcement, emergency response, precision agriculture, mining, finance, and scientific research, among many others (UN Office for Outer Space Affairs, 2025). Another relevant application of this technology, particularly significant for the objectives of this thesis, is its use in meteorology and environmental monitoring to estimate the Zenith Tropospheric Delay (ZTD) (Dabove and Di Pietra, 2024).

1.1.1 GNSS segments

The GNSS architecture is composed of three main segments: the space segment, the control segment, and the user segment (Hofmann-Wellenhof et al., 2008).

- The space segment consists of the satellite constellations that ensure continuous positioning coverage by maintaining a sufficient number of satellites in orbit so that at least four are simultaneously visible from any point on Earth. The primary functions of this segment are to broadcast navigation signals containing precise timing and orbital information referenced to an accurate time scale, and to receive and store data transmitted from the control segment.

- The control segment (also referred to as the ground segment) comprises a network of ground stations responsible for managing and maintaining the entire system. Its main tasks include satellite tracking, ephemeris estimation, clock control, bias correction, orbit control, and uploading updated navigation data to the satellites. Each constellation relies on a dedicated network of control elements, including master control stations, monitoring stations, and uplink antennas that together ensure precise coordination of the operations, collection of tracking data and continuous communication with the satellites.

- The user segment encompasses all GNSS receivers and users capable of acquiring and processing satellite signals. This segment includes both civilian and military users, which can further be classified as authorized or unauthorized, depending on the level of access to system data and services.

1.1.2 GNSS signals and signal multiplexing techniques

The satellites forming GNSS constellations continuously transmit signals in the L-band frequency range, which ranges from 1 GHz to 2 GHz (Campos et al., 2023). These signals are essential for delivering information related to positioning, navigation, and timing. A complete GNSS signal consists of a high-frequency carrier wave that is modulated by both a Pseudo-Random Noise (PRN) code and a navigation message.
The carrier signal is a high-frequency electromagnetic wave that serves as the base for modulation. Its wavelength is typically around 20 cm, depending on the specific transmission frequency.
The Pseudo-Random Noise (PRN) code, also known as the pseudorange code, is a binary sequence composed of +1 and –1 values used to modulate the carrier wave.
The navigation message, also referred to as the broadcast signal, consists of a set of binary codes containing essential information such as satellite orbital parameters

(ephemeris), clock corrections, and system status. It is modulated on top of both the PRN code and the carrier signal (Jin et al., 2021).
Satellite multiplexing refers to the set of techniques that allows multiple satellites to transmit signals simultaneously while allowing receivers to correctly distinguish among them. These methods minimize mutual interference and ensure that the receiver can reliably acquire and identify the signal originating from a specific satellite. The three main multiplexing techniques are Code Division Multiple Access (CDMA), Frequency Division Multiple Access (FDMA), and Time Division Multiple Access (TDMA).
In CDMA, each satellite has a unique identification code, while signals overlap in the frequency and time domains. This approach allows several signals to be transmitted simultaneously over the same carrier frequency providing high spectral efficiency and robustness against interference.
FDMA operates by assigning a distinct carrier frequency to each satellite, so that signals differ in the frequency domain but overlap in both time and code domains. This method facilitates signal separation at the receiver level, although it generally requires more complex and costly receiver and antenna designs.
In TDMA, a specific time slot is assigned to each station. Consequently, each satellite transmits at different time slots. TDMA requires accurate synchronization among the transmitting stations to ensure proper operation (Hofmann-Wellenhof et al., 2008).
Among current global GNSS constellations, all operational systems adopt the CDMA technique, with the exception of GLONASS, which traditionally relies on FDMA. However, the modernization phase of GLONASS includes the implementation of CDMA signals in newer satellite generations to enhance interoperability with other global systems (Ávila Rodríguez, 2011).

1.1.3 Biases in the measurements

All GNSS observables are influenced by a combination of systematic biases and random noise. Systematic effects can be broadly categorized into three main groups: satellite-related biases, propagation-medium-related biases, and receiver-related biases (Hofmann-Wellenhof et al., 2008).

- Satellite-related biases primarily include satellite clock errors and ephemeris (orbit) errors. Although GNSS satellites are equipped with highly stable atomic clocks, small drifts are inevitable and must be accounted for. Orbit errors arise from discrepancies between the satellite's actual trajectory and the broadcast ephemeris. While these deviations are usually minor, they propagate into the user's position solution and can introduce non-negligible errors. Both satellite

clock and orbit errors affect carrier-phase and code measurements in a similar manner (Wells et al., 1999).

- Propagation-medium-related biases include the ionospheric delay and tropospheric delay. The ionosphere extends from approximately 50 km to 1000 km above the Earth and it contains a significant density of free electrons and ions, which alter the refractive index for radio waves, making it a dispersive medium for GNSS signals. The ionospheric delay depends on solar activity, time of day, season, and geographic location, which complicate its estimation (Hofmann-Wellenhof et al., 2008). The tropospheric delay represents one of the most significant error sources in GNSS positioning (Wu et al., 2023). Since it is of primary importance for the purpose of this thesis, it will be discussed in greater detail in the following section.

- Receiver-related biases include antenna phase center variations, receiver clock bias, multipath, and receiver noise. The phase center variation arises because the electrical phase center of the antenna does not coincide with its geometric center, and its position varies depending on the signal's direction of arrival. The receiver clock bias is due to the absence of an atomic clock in typical GNSS receivers, causing the internal time scale to deviate from GNSS system time. Multipath occurs when signals reach the antenna via reflected paths from nearby surfaces such as buildings, vegetation, or rocks, introducing interference in both code and carrier-phase measurements. Finally, receiver noise originates from imperfections in the antenna, cables, and electronic processing, producing small but unavoidable random errors (Hofmann-Wellenhof et al., 2008; Teunissen and Montenbruck, 2017).

Additionally, GNSS observations are affected by hardware biases from both the satellite and the receiver, which influence both carrier-phase and code measurements (Teunissen and Montenbruck, 2017; Meindl, 2011). As will be discussed in the following subsections, many systematic biases can be mitigated or effectively eliminated through linear combinations of measurements or differencing techniques, which are fundamental for achieving high-precision GNSS positioning (Hofmann-Wellenhof et al., 2008).

1.1.4 Positioning techniques

Positioning in GNSS is based on the estimation of the geometric distance between each satellite and the receiver, obtained by multiplying the speed of light by the signal travel time. A wide range of positioning techniques are currently available and they

differ according to several criteria. A first distinction concerns the number of receivers involved, namely single-receiver or multi-receiver configurations. A second classification refers to the different modalities of data elaboration, distinguishing Real-Time from Post-Processing techniques. An additional distinction concerns the measurement types employed, which may rely on code observations, carrier-phase observations, or a combination of both. Below is a brief description of the main positioning techniques.
Stand-Alone Positioning relies exclusively on the information broadcast by the satellites, without the support of any external reference station or correction service. The user position is obtained by combining measurements from multiple satellites (at least four) to determine an absolute location within the selected reference system. Since no differential corrections are applied, systematic errors and biases cannot be removed, which limits the achievable accuracy. Stand-Alone Positioning typically employs code observations and it is performed in Real-Time.
Single Point Positioning (SPP), although often used interchangeably with Stand-Alone Positioning, has a more specific technical meaning. SPP is conventionally defined as single-frequency GNSS positioning that makes use only of code measurements in Real-Time mode. The accuracy depends on the receiver's characteristics, the type of code employed, and the GNSS constellation used. With the GPS C/A code, typical accuracies are on the order of 30 m, whereas the P code allows for reaching approximately 3–5 m under favorable conditions (Zuliani, 2021).
Precise Point Positioning (PPP) is an advanced evolution of SPP that enables centimeter-level accuracy using a single GNSS receiver. PPP exploits carrier-phase measurements and, in most implementations, dual-frequency observations to eliminate the ionospheric delay through linear combinations. Additional error sources, such as tropospheric delay and carrier-phase ambiguities, are explicitly modeled and estimated. This technique requires specific satellite products, namely precise satellite orbits and clock corrections, provided by international GNSS analysis centers. PPP solutions are characterized by a convergence period, which is the time required for the solution to reach its full precision. Typical convergence times are about 30 minutes, which can be reduced to approximately 20 minutes using multi-frequency and multi-constellation receivers. Multi-constellation PPP is also advantageous in environments where vegetation or tall buildings partially obstruct satellite signals. PPP can be applied to both static and kinematic platforms (Teunissen and Montenbruck, 2017).
Relative Positioning involves determining the position of one or more rover receivers with respect to a reference station of known coordinates. While the reference station remains fixed, the rover(s) may be either static or in motion. The objective is to estimate the vector separating the two points, known as the baseline, which provides a relative

position of the rover with respect to the reference station through simultaneous observations. This takes advantage of the fact that many errors (ionosphere, troposphere, satellite clock errors, similar local multipath) are almost equal at both points if the distance is limited. This approach enables the elimination of the bias through single, double, or triple differences of observations. Relative Positioning predominantly relies on carrier-phase measurements due to their higher precision, but also on pseudorange measurements (Teunissen and Montenbruck, 2017; Zuliani, 2021). Differencing techniques are mathematical tools used to combine observations from multiple receivers. The primary objective is to reduce measurement biases through a process called differencing, which is applied in both pseudorange and carrier-phase GNSS observations. As already mentioned, differencing can be classified into single, double, or triple differences.

- Single differences are of two types: between-receivers single difference and between-satellites single difference. Both require simultaneous observations and reduce biases, though they do not eliminate them completely. Between-receivers single difference involves two receivers observing the same satellite. Two measurement equations are written, which are then combined into a single difference equation. The satellite clock bias cancels out because it is the same for both receivers. Additionally, for baselines up to 15–20 km, atmospheric biases and orbital errors are largely canceled due to the relative proximity of the receivers. The remaining unknowns are receiver coordinates, combined clock offset, and combined phase ambiguities. This technique enables centimeter-level carrier-phase positioning for baselines around 10 km and meter-level pseudorange positioning for baselines of several hundred kilometers (Van Sickle, 2023). In between-satellites single difference there is a single receiver observing two satellites simultaneously. Measurements are subtracted, which cancels the receiver clock error and reduces ionospheric and tropospheric delays. However, this method does not significantly improve positioning accuracy beyond what is achievable with standard SPP.

- The double difference combines the two types of single differences, using two satellites and two receivers. Four measurement equations lead to a single double-difference equation. In this process, satellite and receiver clock errors are removed, and ionospheric and tropospheric errors are reduced. The remaining unknowns are the receiver coordinates and combined phase ambiguities.

- A triple difference is obtained by differencing two double differences at different epochs. This cancels the effect of phase ambiguities but generally produces less accurate solutions. Since it requires measurements at different times, it cannot be

used for Real-Time Positioning. Also known as the between-epochs difference, this technique is particularly useful for detecting and repairing cycle slips in carrier-phase measurements (Van Sickle, 2023).

1.1.5 Low-Cost and High-Cost networks of receivers

As previously discussed, each GNSS constellation is supported by its own dedicated network of ground stations, collectively referred to as the control segment, which is responsible for monitoring, managing, and maintaining the overall functionality of the system. Beyond official control networks, several GNSS receiver networks have been developed by universities, government agencies, space organizations, and geodetic institutions to serve civilian and scientific objectives. These permanent stations enable high-precision position monitoring, provide differential corrections, and support a wide range of scientific and geodetic applications, such as observing crustal deformation and estimating the amount of precipitable water vapor in the atmosphere (Guerova et al., 2016). These high-grade infrastructures are not homogeneously distributed around the world, specifically in developing countries, and installation cost of one receiver is relatively high, around €20,000 for professional surveying receivers and €5,000 - €12,000 for single-frequency receivers (Weston and Schwieger, 2014). Examples of such networks include the EUREF Permanent GNSS Network (EPN) and the International GNSS Service (IGS) network.

The EUREF Permanent Network is a continuously operating complex of more than 330 multi-GNSS reference stations distributed throughout Europe and coordinated by the EPN Central Bureau. Originally established to support and enhance the maintenance of the European Terrestrial Reference System (ETRS89) and its successive realizations, the network now plays a key role in the modernization of European permanent GNSS infrastructures. The EPN operates through the voluntary collaboration of more than 130 contributing organizations and agencies. The network's stations generate daily data products, nearly all of which supply hourly observations, and roughly half are capable of Real-Time data transmission. Approximately 30% of EPN stations are also integrated into the IGS network (Bruyninx et al., 2019). **Figure 1.1** shows the spatial distribution of EUREF stations.

The IGS operates a worldwide network of over 500 permanent GNSS reference stations that continuously record high-precision observations. This infrastructure supports the realization and maintenance of the International Terrestrial Reference Frame (ITRF) by providing precise GNSS-derived coordinates, station velocities, and Earth Rotation Parameters (ERPs). Created under the coordination of the International Association of Geodesy (IAG), the IGS is managed through the collaboration of scientific institutions,

academic organizations, and government agencies worldwide. All IGS data products are openly accessible and provide high-accuracy information essential for geodetic, geophysical, and environmental research (Global Geodetic Observing System, 2025).

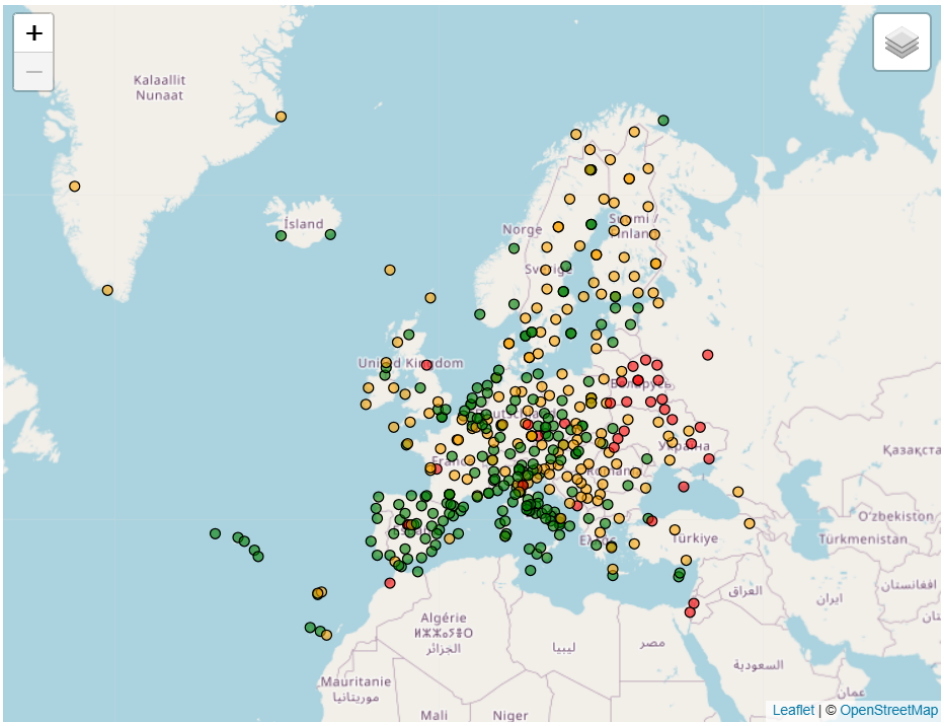

Figure 1.1: Spatial distribution of the EUREF Permanent Network (EPN) stations across Europe (Bruyninx et al., 2019).

Centipede RTK network is an open-source, global infrastructure composed of permanent, low-cost GNSS stations, initially deployed in France in 2019. The network operates within a collaborative community framework that allows users to collect, share, and access real-time GNSS observation data from all connected stations. The initiative is supported through a combination of public and private funding sources (Centipede RTK Project, 2025). Several studies have demonstrated the positioning performance of these low-cost GNSS receivers, both under static and kinematic conditions (Garrido-Carretero et al., 2019; Wu et al., 2025). Furthermore, recent investigations have highlighted the potential of these low-cost receivers to effectively monitor atmospheric water vapor variability and to provide accurate estimates of the ZTD (Bosser et al., 2024; Dabove and Bagheri, 2023). These findings highlight the potential of low-cost GNSS technology for enhancing spatial coverage in regions lacking high-cost reference networks, as well as for densifying existing infrastructures to improve the overall precision and reliability of geodetic measurements. **Figure 1.2** shows the spatial coverage of Centipede stations used in this study.

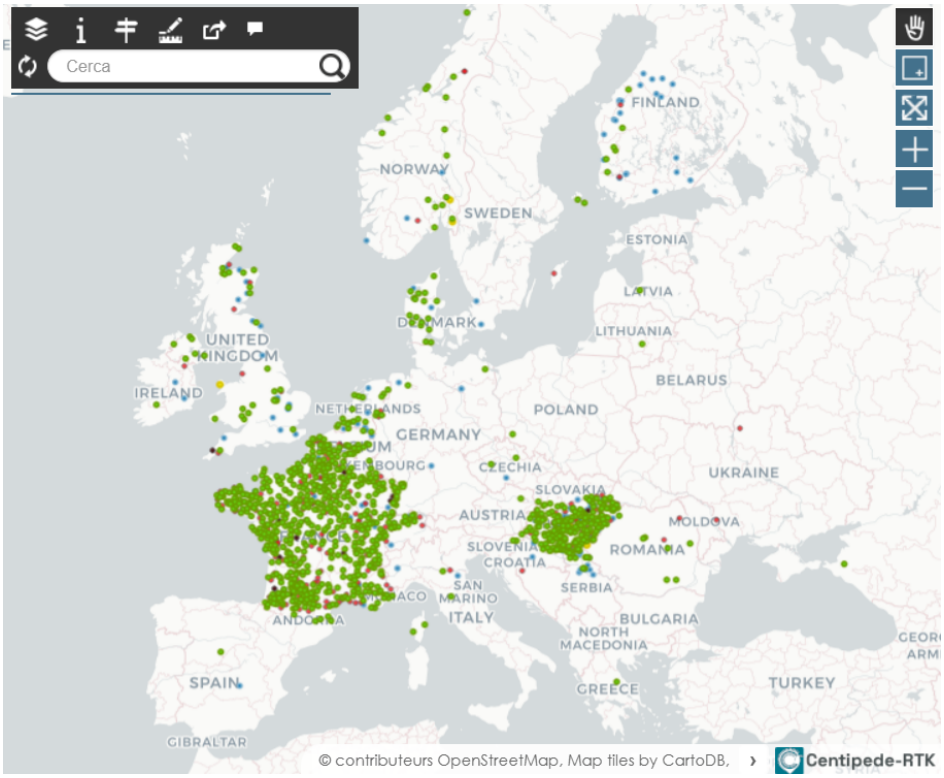

Figure 1.2: Spatial distribution of the Centipede RTK Network stations across Europe (Centipede RTK Project, 2025).

1.2 Zenith Tropospheric Delay (ZTD)

The pseudorange observation equation, denoted as P_r^s, is the following, where the satellite is abbreviated as s and the receiver as r:

$$P_r^s = \rho_r^s + c(dt_r - dt^s) + T_r^s + I_r^s + e_r^s \tag{1.1}$$

In this formulation, ρ_r^s represents the geometric distance, c is the speed of light in vacuum, dt_r refers to the reparametrized receiver clock offset, while dt^s is the satellite clock offset; together, $c(dt_r - dt^s)$ accounts for the synchronization errors or clock offsets, of both the receiver and the satellite. The atmospheric effects are introduced through the tropospheric delay T_r^s, and the ionospheric delay I_r^s. Finally, e_r^s represents the pseudorange receiver noises, multipath and other small effects.
The carrier-phase observation ϕ_r^s, expressed in units of length, follows a similar formulation but includes an additional ambiguity term, and is given by:

$$\phi_r^s = \rho_r^s + c(dt_r - dt^s) + T_r^s - I_r^s + \lambda N_r^s + \epsilon_r^s \tag{1.2}$$

Beyond the geometric and clock terms already described for the pseudorange, this equation includes the integer phase ambiguity N_r^s multiplied by the signal wavelength λ. The phase ambiguity represents the unknown number of full cycles between the satellite and the receiver at the moment of signal acquisition. N_r^s remains constant in the absence of cycle slips, provided that continuous satellite tracking is maintained. The term ϵ_r^s represents the phase-specific measurement noise, which allows for millimeter-level precision once the phase ambiguity is correctly resolved (Teunissen and Montenbruck, 2017).

Tropospheric delay (T_r^s) is of particular interest for the purpose of this thesis. It refers to the delay that GNSS signals experience while passing through the neutral atmosphere. This phenomenon is primarily caused by the atmospheric refractivity. Neutral atmosphere refers to the portion of the atmosphere that is essentially non-dispersive for electromagnetic waves with frequencies up to 15 GHz. It comprises the troposphere and the stratosphere, extending approximately from 0 to 50 km above the Earth's surface. In GNSS terminology, this region is often simply referred to as the troposphere, and the associated signal delay is called the tropospheric delay, since the troposphere is the layer that contributes most significantly to this effect (Hofmann-Wellenhof et al., 2008). It is divided into tropospheric hydrostatic delay and tropospheric wet delay. The first part accounts for about 90% of the total delay and can be reliably estimated using empirical models as it primarily depends on the dry constituents of the atmosphere. Instead, the wet delay is significantly more challenging to characterize due to the high spatial and temporal variability of water vapor (Ma et al., 2021). The refractive index of the troposphere depends on atmospheric pressure p, temperature T, and the partial pressure of water vapor e.

The total atmospheric refractivity, N_{tot}, is composed of a dry component (N_{dry}) and a wet component (N_{wet}). It can be expressed according to the Smith-Weintraub formulation as:

$$N_{\text{tot}} = N_{\text{dry}} + N_{\text{wet}} = k_1 \cdot \frac{p - e}{T} + k_2 \cdot \frac{e}{T} + k_3 \cdot \frac{e}{T^2}, \tag{1.3}$$

where k_1, k_2, k_3 are empirical constants specific to the atmospheric constituents and are given by $k_1 = 77.689\ \text{K} \cdot \text{hPa}^{-1}$, $k_2 = 71.2952\ \text{K} \cdot \text{hPa}^{-1}$, and $k_3 = 375,463\ \text{K}^2 \cdot \text{hPa}^{-1}$ (Wilgan et al., 2017).

The total tropospheric delay T_r^s can be expressed with the following equation:

$$T_r^s = 10^{-6} \int_r^s N \, dw \tag{1.4}$$

where w denotes the propagation path traveled by the signal from the receiver to the satellite.

The previous equation can be expanded as follows:

$$T_r^s = 10^{-6} \int_r^s N_{dry}, dw + 10^{-6} \int_r^s N_{wet}, dw \tag{1.5}$$

where the total delay is expressed as the sum of two distinct line integrals (Dabove and Bagheri, 2023). The tropospheric delay is typically categorized into two types depending on the signal's geometry: Zenith Tropospheric Delay (ZTD) and Slant Tropospheric Delay (STD).
ZTD is the delay experienced by GNSS signals traveling in the zenith direction with respect to the receiver. Physically, it is decomposed into the Zenith Hydrostatic Delay (ZHD) and the Zenith Wet Delay (ZWD):

$$\text{ZTD} = \text{ZHD} + \text{ZWD} \tag{1.6}$$

On the other hand, the STD represents the delay occurring along the actual signal propagation path between the satellite and the receiver at a specific elevation angle (e). The STD is related to its zenithal components through the application of mapping functions (m):

$$\text{STD} = m_h(e) \cdot \text{ZHD} + m_w(e) \cdot \text{ZWD} \tag{1.7}$$

where $m_h(e)$ and $m_w(e)$ denote respectively the hydrostatic and wet mapping functions (Won et al., 2010).

1.3 Integrated Water Vapor (IWV)

The Integrated Water Vapor (IWV), also known as Total Column Water Vapor, represents the total mass of water vapor contained within a vertical atmospheric column of unit cross-sectional area, extending from the Earth's surface to the top of the atmosphere. It is typically expressed in units of mass per area (kg/m^2) or, equivalently, as the height of the corresponding column of liquid water (mm).
Traditionally, IWV measurements were obtained with radiosondes, which are weather balloons equipped with sensors that capture humidity, temperature, and pressure. Despite their accuracy, radiosondes suffer from limited temporal sampling and high maintenance costs, as they can only provide data during specific launch intervals, typically occurring twice a day. To overcome these issues, IWV is increasingly monitored through GNSS-based atmospheric sensing, which calculates the excess delay experienced by signals as they propagate through the tropospheric water vapor. This estimation process is complex, as it requires the precise isolation of the wet delay from other delays.

Atmospheric water vapor is primarily concentrated within the lowest 4 km of the troposphere, specifically in the Planetary Boundary Layer. Its distribution exhibits extreme spatiotemporal heterogeneity, driven by local evaporation and turbulent mixing. This high degree of variability poses significant challenges for its accurate characterization and prediction using traditional meteorological models. For instance, its magnitude could undergo rapid fluctuations, potentially doubling within a few hours due to the collision of two air masses with different temperature and humidity (Teunissen and Montenbruck, 2017). At mid-latitudes, the general seasonal trend of IWV is characterized by peak values during the summer and minimum values in winter (Bosser et al., 2024).

The retrieval of high-resolution IWV data is fundamental for enhancing Numerical Weather Prediction (NWP) models, investigating the global hydrological cycle, and analyzing atmospheric radiative properties (Rohm et al., 2014). As it is one of the most important drivers of troposphere dynamics, the knowledge of its short-periodic variations helps NWP while measuring long-periodic variations improves climate modeling (Hofmann-Wellenhof et al., 2008). Extensive literature has documented the critical role of water vapor in driving precipitation dynamics. There are studies that have proven the correlation between the increase in IWV before high rainfall events up to 40-50 mm (Rohm et al., 2014; Brenot et al., 2006; Champollion et al., 2004; Choy et al., 2013). This relationship was further documented by Van Baelen et al. (2011), who demonstrated that frontal systems develop preferentially in environments with high water vapor and that elevated water vapor concentrations act as a primary precursor for the initiation of local convection.

Water vapor is also a key factor in climate research because it acts as a major greenhouse gas. Studies have shown its high impact on the atmosphere; for example, a 20% increase in IWV in the tropics can affect the Earth's climate more than doubling the CO_2 concentration. This makes the ability to monitor water vapor through GNSS an essential tool for understanding climate change and how the atmosphere responds to warming (Teunissen and Montenbruck, 2017).

Chapter 2

Objectives of the thesis

In the field of GNSS meteorology, the emergence of low-cost GNSS receivers is really promising for densifying Integrated Water Vapor (IWV) observations, which can improve the accuracy of climate modeling and can be assimilated into meteorological prediction.

While current literature extensively focuses on accuracy evaluation of Zenith Tropospheric Delay (ZTD) estimates through low-cost GNSS networks like Centipede, few studies extend this analysis to the retrieval and validation of IWV. This work addresses this gap by implementing a complete operational framework, transitioning from raw tropospheric delay estimations to the generation and validation of interpolated IWV products.

A crucial aspect of this research involves evaluating how IWV estimates are influenced by elevation and spatial distribution of GNSS stations. While traditional studies mostly rely on Ordinary Kriging or on other interpolation techniques, the implementation of External Drift Kriging (EDK) for IWV remains relatively rare. This choice is fundamental especially in areas with complex orography, characterized by both mountains and valleys.

Regarding the structure of the thesis, chapter 3 presents the methodology adopted. It begins with the data acquisition part, detailing the chosen dataset, the study area, and the observation period. This is followed by a description of the data processing phase, including an overview of the type of software used for the Precise Point Positioning (PPP) technique. The core of the analysis focuses on the description of the equations used for the retrieval of IWV and the search for required parameters for the computation. Finally, the chapter describes the geostatistical framework of EDK, along with its validation through computation of RMSE and bias.

Chapter 4 presents the key results obtained in the analysis. Initial findings include daily and weekly tropospheric delay time series, followed by a dedicated elevation de-

pendency study to investigate the impact of topography on the estimates. The analysis then shows spatial distribution and temporal evolution of water vapor, using interpolated maps obtained through EDK. Additionally, the chapter investigates the spatial correlation of IWV through experimental and theoretical variograms. The accuracy of the estimates is represented by the results of Leave-One-Out cross-validation and Independent External Validation, which compares the network's performance against high-resolution permanent stations.
Chapter 5 provides a comprehensive discussion of these findings, contextualizing the results within the framework of existing literature and proposing future perspectives.

Chapter 3

Methodology

This chapter presents the methodology adopted for the study, detailing the software tools, the processing strategies, and the derivation of the atmospheric parameters essential for the analysis. Specifically, GNSS observations from the low-cost Centipede RTK network are processed to obtain the ZTD. These estimates are subsequently utilized to compute the IWV. Finally, the spatial distribution of water vapor is analyzed by generating interpolation maps through the External Drift Kriging technique.
The computational analysis and geostatistical modeling were conducted using MATLAB, whereas the spatial distribution map of the GNSS stations was generated using QGIS.

3.1 Data acquisition

The GNSS data utilized in this study were retrieved from the open-source Centipede RTK GNSS network. The selected 13-station network is located in Southeastern France, covering a total area of approximately 23,000 km^2. The study area is characterized by a significant topographic diversity, with ellipsoidal heights ranging from 170 m (station GROF) to 2,328 m (station SCV1). This altimetric range is fundamental to the analysis, as it allows for a detailed investigation of the vertical distribution and stratification of atmospheric water vapor. Distances from neighboring stations range from 20 to 60 km.
Each station is equipped with a u-blox multi-band (L1, L2) and multi-constellation receiver, capable of tracking GPS, GLONASS, Galileo, BeiDou, and SBAS signals.
Table 3.1 provides the geographic coordinates (latitude and longitude) and the ellipsoidal heights for each site. All spatial data are referenced to the RGF93 (Réseau Géodésique Français 1993) geodetic datum.

Station ID	Latitude [°]	Longitude [°]	Ellipsoidal height [m]
CARC	45.11411491	4.96849173	250.139
CRO2	45.27177065	5.89140627	285.471
CVRA	44.92751974	4.92284897	223.200
EOAA	45.24951373	4.98769774	367.156
GRME	44.23192521	5.47592105	950.239
GROF	44.49174602	4.75177369	170.945
GRPE	44.70859304	5.38390881	550.033
LORI	44.73864386	4.99102254	230.117
PALLU	45.68537952	6.39368072	527.378
SCV1	44.92015323	6.54955394	2328.527
TD04	44.24876765	5.86193952	622.821
TDPT	44.78779823	6.53966498	1356.543
TMAC	45.20849094	5.79335930	276.046

Table 3.1: Summary of the geographic locations and ellipsoidal heights for the 13 GNSS sites analyzed. Coordinates are expressed in the RGF93 geodetic datum.

The spatial distribution of the stations across the study region is illustrated in **Figure 3.1**.

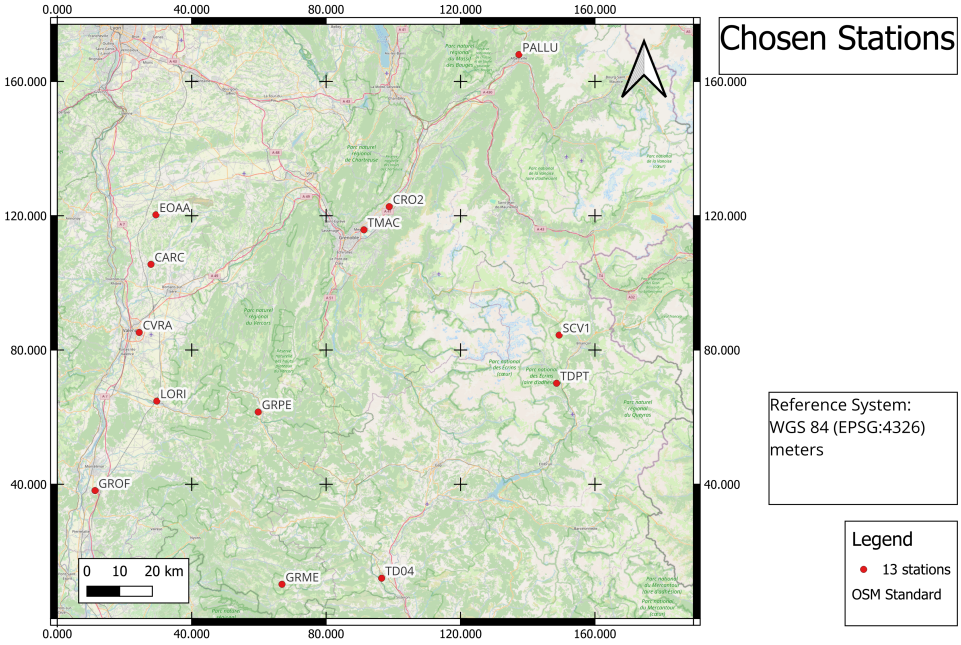

Figure 3.1: Geographical distribution of the 13 GNSS stations within the study area in Southeastern France.

The selected network follows a distinct altimetric gradient, which is essential for sampling different layers of the troposphere. The highest stations, SCV1 (2,328 m) and

TDPT (1,356 m), are situated in the High Alps; these sites are characterized by lower temperatures and a reduced atmospheric column, resulting in naturally lower IWV values. At intermediate altitudes, stations such as TMAC, CHAL, and LORI are located within the Pre-Alps and transition zones, where orographic effects often influence moisture distribution. Finally, the network includes stations located in the major valley corridors, such as GROF, CVRA, and CARC. These low-elevation sites (ranging from 170 m to 250 m) are characterized by higher temperatures and pressure, acting as reservoirs for atmospheric water vapor due to their proximity to the Rhône river and Mediterranean air mass inflows. The network also includes a variety of anthropogenic environments, ranging from isolated rural sites to densely populated urban areas (like Grenoble). Due to the Urban Heat Island effect, cities typically maintain higher temperatures than their rural surroundings (Held and Soden, 2000). According to the Clausius-Clapeyron principle, this increased thermal energy enhances the atmosphere's capacity to hold moisture, often resulting in higher localized IWV values in urban centers.

The dataset analyzed in this thesis covers a one-week period, from 19 July 2025 to 25 July 2025. This time window was selected to investigate the variability of atmospheric water vapor over the study area during a representative summer period in France.

The GNSS network provides high-resolution observations with a sampling interval of 30 s, enabling the detection of short-term variations in the parameters of interest. For each of the 13 stations considered, the key tropospheric parameters available are the ZHD and the ZWD. Their sum yields the ZTD. These parameters constitute the basis for the subsequent conversion into IWV, performed using auxiliary meteorological information derived from the ERA5 reanalysis dataset.

The data recorded by the Centipede stations consist of raw GNSS observations in RINEX (Receiver Independent Exchange) format. For each of the 13 stations involved in the study, a dedicated RINEX file was retrieved for each day of the 7-day analysis period. RINEX is the standard format of GNSS raw data, designed to share and store observation and navigation data between all users and software.

3.2 Data processing

Several processing strategies are reported in the literature; in this study, the Canadian Spatial Reference System (CSRS) processing service was adopted to process raw GNSS data. CSRS provides an open-source, fast, and user-friendly solution that performs Precise Point Positioning (PPP) processing. Unlike other approaches, such as RTKLIB, which requires external acquisition of correction products from third-party

sources (e.g., NASA), the CSRS-PPP service internally supplies the necessary correction data through its own infrastructure. A limitation of this approach is that key processing choices, such as correction products, quality control procedures, and ionospheric modeling strategies, are predefined by the system and are not fully transparent to the user. Nevertheless, for the objectives of this thesis, the accuracies of the resulting products are considered sufficient, as demonstrated in previous studies (Dabove and Bagheri, 2023).

To mitigate the dispersive effects of the ionosphere, the Ionosphere-Free (IF) linear combination is employed. This combination effectively eliminates the first-order ionospheric delay, allowing for a more accurate estimation of the ZTD (Mendez Astudillo et al., 2018).

The GNSS data were processed using post-processing mode through the CSRS-PPP service. Precise Point Positioning was selected over other positioning strategies since recent literature has proven its superior performance in retrieving tropospheric parameters. Relative positioning based on double-differenced observations with fixed ambiguities is often more susceptible to ZTD outliers and exhibits higher noise levels in the resulting time series compared to the PPP approach (Stępniak and Paziewski, 2022). After registering for a free subscription, RINEX data can be uploaded to the CSRS website. The processing was configured in static mode and the temporal reference was aligned with the GPS epoch of the observation data. A 7.5° elevation cut-off angle was used.

The CSRS processing output is sent via email and is provided as a compressed archive containing several files. Among these, the file with the .tro extension is of primary interest, as it contains ZHD, ZWD, and tropospheric gradients for each epoch processed. Technical metadata, estimation accuracy, and satellite tracks are summarized in a .pdf report, along with other important information. The other files include a .csv document and a .pos file containing the positioning and clock information for each processed epoch. The .sum file offers a summary of the PPP processing parameters and the .clk file provides the receiver clock offsets and their associated 95% confidence intervals.

Following the data processing phase, a time series analysis was conducted to evaluate the temporal evolution of the estimated parameters. This approach facilitates a clear interpretation of the atmospheric dynamics and the stability of the retrieved values over the observation period.

3.3 Retrieval of Integrated Water Vapor (IWV)

In GNSS meteorology IWV is not measured directly but is derived from the ZWD. The conversion is defined by the following linear relationship (Wu et al., 2023):

$$IWV = Q \cdot ZWD \tag{3.1}$$

The dimensionless conversion factor, Q, is computed using the following formula (Wu et al., 2023):

$$Q = \frac{10^6}{\rho_w R_w \left(\frac{k_3}{T_m} + \left(k_2 - k_1 \frac{M_w}{M_d}\right)\right)} \tag{3.2}$$

The physical constants and variables involved in the determination of Q are: ρ_w (density of liquid water) = $997\, kg \cdot m^{-3}$; R_w (specific gas constant for water vapor) = $461.525\, J \cdot kg^{-1} \cdot K^{-1}$; $k_1 = 0.776890\, K \cdot Pa^{-1}$; $k_2 = 0.712952\, K \cdot Pa^{-1}$; $k_3 = 3754.63\, K^2 \cdot Pa^{-1}$; M_w (molar mass of water vapor) = $15.9994\, g \cdot mol^{-1}$; M_d (molar mass of dry air) = $28.9644\, g \cdot mol^{-1}$; T_m = weighted mean temperature of the atmosphere [K]. The weighted mean temperature, T_m, is the only variable in the conversion process and represents the average temperature weighted by the vertical profile of water vapor partial pressure. Under the theoretical assumption of an isothermal atmosphere, where the temperature remains constant with altitude, T_m would coincide exactly with the surface temperature (T_s). However, since the actual troposphere exhibits a temperature lapse rate different from zero, T_m must be estimated.
The formal definition of T_m is given by the vertical integral (Bevis et al., 1992):

$$T_m = \frac{\int \frac{e}{T} dz}{\int \frac{e}{T^2} dz} \tag{3.3}$$

where e is the water vapor pressure [Pa] and T the absolute temperature [K].
The formal definition of T_m requires the numerical integration of vertical atmospheric profiles of temperature and water vapor pressure; such high-resolution data are often difficult to obtain with the necessary temporal frequency at specific GNSS site locations. The use of a linear formulation significantly increases computational efficiency while maintaining high accuracy, as it is considered the standard model for mid-latitude regions. For the purposes of this study, T_m was estimated using the empirical relationship proposed by Bevis et al. (1992). The T_m values were computed as follows:

$$T_m = 70.2 + 0.72 \times T_s \tag{3.4}$$

where T_s is the surface temperature [K]. The surface temperature data were retrieved from the ERA5 reanalysis dataset via the Copernicus Climate Data Store. Specifically, the "hourly data on single levels" dataset was utilized to extract the 2 m temperature variable (T_{model}) with an hourly temporal resolution (Hersbach et al., 2023).
The ERA5 reanalysis provides the geopotential (z) expressed in m^2/s^2. To obtain the elevation in units of length, the geopotential needs to be divided by the standard acceleration of gravity (g) as follows:

$$H_{\text{model}} = \frac{z}{g} \tag{3.5}$$

where g is defined as 9.80665 m/s^2. This step ensures that the model topography is expressed in meters, allowing for a direct altimetric comparison with the H_{GNSS} heights of the Centipede stations.
To ensure temporal synchronization with the ZWD observations provided by the Centipede RTK Network, which are sampled every 30 seconds, the hourly ERA5 temperature data were interpolated using a cubic spline interpolation. This method was chosen to maintain a smooth and continuous thermal profile between the discrete hourly nodes.
Before computing IWV, it is essential to account for the altimetric discrepancies between the ERA5 model grid and the GNSS stations. Since atmospheric parameters vary significantly with altitude, considering the model and the receivers at the same elevation would introduce systematic biases, leading to an overestimation or an underestimation of IWV. To mitigate this, a vertical temperature correction was applied using the following equation:

$$T_s = T_{model} + \Gamma \cdot (H_{GNSS} - H_{model}) \tag{3.6}$$

where T_s [K] is the surface temperature adjusted to the actual station elevation; T_{model} [K] is the 2 m surface temperature provided by the ERA5 reanalysis at the model grid height; (H_{model}) is the model grid height; H_{GNSS} [m] is the ellipsoidal height of the GNSS receiver, and Γ is the environmental lapse rate, assumed to be -0.0065 K/m (Jade and Vijayan, 2008).
The resulting corrected temperature (T_s) was used to calculate the weighted mean temperature (T_m) via the Bevis formula (**Equation (3.3)**). This parameter was then integrated with the ZWD values to derive high-resolution IWV estimates at 30-second intervals for all selected stations throughout the analysis period with **Equation (3.2)** and **Equation (3.1)**.

3.4 Spatial interpolation

Spatial interpolation is an essential tool for atmospheric monitoring, as it allows for the transition from discrete to continuous information. To optimize spatial interpolation strategy, the vertical distribution of tropospheric delays and of water vapor was studied. This was useful to prove that both exhibit a clear dependence on elevation. This justifies the choice of an interpolation model that considers elevation as a secondary variable in the process.

To achieve spatial homogeneity and estimate values of IWV in areas without GNSS coverage, Kriging was performed, allowing the passage from point-based observations to continuous spatial information. Kriging interpolation is a widely recognized technique used in fields such as geography, geodesy, geology and environmental science, which provides the Best Linear Unbiased Estimation (BLUE). It operates under two theoretical assumptions: first, the physical value of a variable measured in a place is not independent from the physical value of a variable measured nearby (spatial correlation assumption), secondly, this correlation weakens as the distance increases (distance correlation assumption).

Given the high correlation between topography and water vapor distribution, it was decided to consider elevation as a variable for the interpolation and to use External Drift Kriging (EDK), which represents an important geostatistical tool. In this way, the model considers elevation as a guide variable in the spatial estimation of IWV (Hohn, 1991).

The first step in quantifying spatial variability was the computation of the experimental variogram. Spatial autocorrelation between the 13 GNSS stations was evaluated and then incorporated into the prediction of unknown values at unsampled locations. The semivariance was computed with the following formulation:

$$\gamma(h) = \frac{1}{2N(h)} \sum_{i=1}^{N(h)} [z(x_i) - z(x_i + h)]^2 \tag{3.7}$$

In this expression, $\gamma(h)$ represents the semivariance at a specific lag distance h, while $N(h)$ denotes the total number of pairs of observation points separated by that distance. The term $z(x_i)$ is the measured value of the variable at location x_i and $z(x_i+h)$ indicates the values of the variable measured at the location $x_i + h$ (Akar and Inal, 2024).

By plotting the semivariance against the lag distance, an experimental semivariogram is obtained, that in the field of geostatistics is simply called "variogram". Then different theoretical models were tried and the one that fitted best the experimental data

was chosen. This is the theoretical variogram. There are three essential parameters that characterize the theoretical variogram: the sill, the range and the nugget. The sill corresponds to the horizontal asymptote and represents the maximum value of correlation present between the observation points. The range is the lag distance at which the variogram reaches the sill and defines the maximum distance of correlation. Finally, the nugget is the interception between the variogram and the y axis, accounts for the natural difference between two measurements taken at the same location; ideally it should be close to zero.
With a network of 13 stations, the number of unique couples identified was 78. To create a clearer visualization, the distances were binned into 8 intervals. The maximum inter-station distance was divided into 8 equal intervals and each pair was assigned to the corresponding interval. For each interval, local means of the distances and of the semivariances were computed and used to create the theoretical variogram. These means are the points visible in the graph.
As previously noted, External Drift Kriging was chosen. EDK is a variant of kriging with a deterministic trend model and it allows the inclusion of a secondary variable in the estimation of a primary variable (Deutsch and Journel, 1997). In this technique, the trend is modeled as a linear function of a secondary external variable, which in the case of the thesis is elevation (Goovaerts, 1997). Since the EDK algorithm operates directly on geographic coordinates, which are directly supplied by the Centipede infrastructure, no further coordinate transformation was needed. Two essential conditions must be satisfied to implement EDK: (i) the external variable must vary smoothly in space, and (ii) it must be known at all locations within the study area (Deutsch and Journel, 1997). Both these conditions are met in the case study.
Finally, EDK algorithm was implemented in MATLAB to obtain a continuous, high-resolution distribution of IWV. EDK was performed at a six-hour interval (four times for each day), achieving a balance between capturing diurnal temporal changes and maintaining a manageable volume of data. This approach resulted in a total of 28 atmospheric maps covering the entire observation period. The outputs will be maps with the spatial distribution of IWV values in the study area. Topographic contour lines were overlaid on the resulting spatial distributions to facilitate the visualization of the correlation between IWV and altitude.

3.5 Validation and RMSE analysis

To evaluate the accuracy of the interpolation model, both internal and external validation procedures were performed.

The assessment began with an internal Leave-One-Out cross-validation. In each iteration, one station was removed from the interpolation process and External Drift Kriging was done using the remaining 12 stations. The estimated and the observed values of IWV were compared through the computation of Root Mean Square Error (RMSE):

$$\text{RMSE} = \sqrt{\frac{1}{n}\sum_{i=1}^{n}(IWV_{\text{est},i} - IWV_{\text{obs},i})^2} \tag{3.8}$$

Where (IWV_{est}) is the value IWV estimated by the interpolation model and (IWV_{obs}) is the IWV measured by the GNSS station. RMSE is a key statistical tool that measures the overall magnitude of prediction errors, with lower values indicating better performance and vice versa.

The systematic component of the error was assessed through the bias:

$$\text{Bias} = \frac{1}{n}\sum_{i=1}^{n}(IWV_{\text{est},i} - IWV_{\text{obs},i}) \tag{3.9}$$

A positive bias shows a tendency of the model toward overestimation, while a negative value suggests underestimation. A value of the bias close to zero means that the model is free of systematic biases.

To enhance the reliability of the analysis, the results were also compared to EUREF Permanent Network data through an additional validation. This external comparison gives robustness to the study, as EUREF stations utilize high-cost, high-precision permanent instrumentation that represent the European standard for geodetic and meteorological quality. Unlike internal cross-validation, this independent assessment is completely decoupled from the interpolation model, offering an objective verification of the physical consistency of the results and is therefore more valuable.

Since the nearest available EUREF station, BRMS (Lyon) **Figure 3.2**, is situated outside the study area, a fourteenth station from the Centipede RTK Network was added to the primary network toward Lyon, thereby reducing potential extrapolation errors and ensuring a more reliable performance assessment.

The validation target is the EUREF station located in Lyon (BRMF) with the following coordinates: latitude 45.72° N, longitude 4.94° E, and ellipsoidal height $h = 248.8$ m, referenced to the RGF93 (Réseau Géodésique Français 1993) geodetic datum.

Since official post-processed data available in the EUREF portal do not provide ZWD, which is essential for the computation of IWV, raw GNSS data were processed autonomously. To maintain strict methodology consistency, CSRS-PPP service was preferred, following the same procedure used for the 13 study stations. As the EUREF

sampling frequency of 30 seconds matches the one of Centipede receivers, no adjustment in the frequency of data was necessary. The IWV for BRMF station were then computed as described in the previous section.
The additional Centipede station, identified as COMBE, is located at latitude 45.8984° N, longitude 4.8201° E, with an ellipsoidal height of 238.0 m, referenced to the RGF93 (Réseau Géodésique Français 1993) geodetic datum. Its position can be seen in **Figure 3.2**. The IWV time series for this station was computed by applying the same methodological process used for the rest of the network.

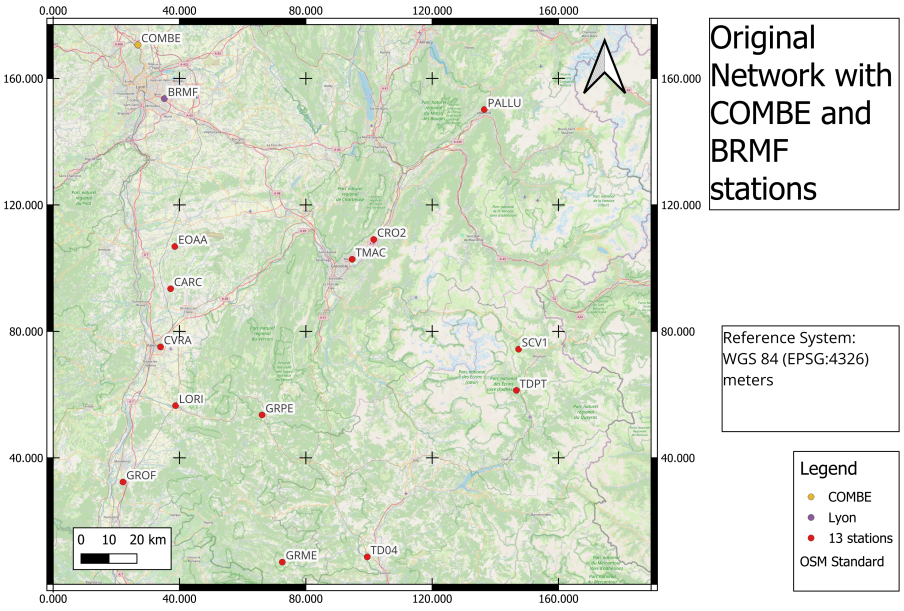

Figure 3.2: Geographical layout of the GNSS network, including the EUREF permanent station BRMF (Lyon) and the Centipede RTK station COMBE.

An external validation was then performed by training the interpolation model using IWV from the new 14 observation points and predicting the value at Lyon. The ground-truth measured value was subsequently compared to the estimated one through the computation of RMSE (**Equation (3.8)**) and bias (**Equation (3.9)**). The decision to perform an external validation against the EUREF Permanent Network EPN is a essential for this thesis. While internal cross-validation assesses the model's consistency, external validation provides an absolute quality assurance.

Chapter 4

Results

This chapter presents the experimental findings of the study. The analysis begins with a temporal visualization of the tropospheric delays retrieved from low-cost GNSS receivers, evaluated at both daily and weekly scales. Subsequently IWV values computed through the combination of ZWD estimates from the Centipede RTK network and ERA5 temperature values are analyzed with their respective time series.
The analysis then moves to the survey of IWV spatial distribution through the results of the External Drift Kriging procedure.
Finally, to assess the robustness of the work, the proposed methodology is validated using both Leave-One-Out cross-validation technique and External Validation by comparing the retrieved IWV estimates against the EUREF measurements.

4.1 Tropospheric delay analysis

This section details the results obtained from the processing of GNSS data collected across the 13-station network. To avoid redundant visualization, a selection of the most relevant graphical outputs is presented. To show the temporal evolution of both ZTD and ZWD, a time series analysis approach is adopted. This covers daily variations and shows the weekly trend of tropospheric delays. Lastly, the physical correlation between station elevation and tropospheric parameters is highlighted.

4.1.1 Tropospheric delay time series

Initially, tropospheric delay time series were generated to visualize their temporal variability across the network.

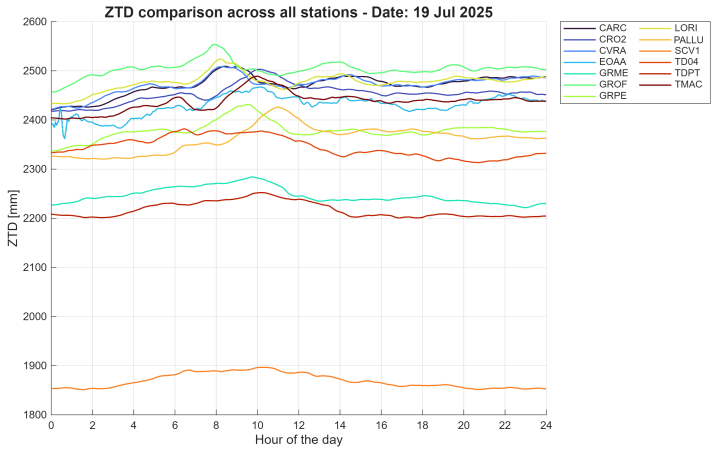

Figure 4.1: Daily time series of ZTD across the 13 GNSS stations (19 July 2025).

Figure 4.1 shows the Zenith Tropospheric Delay variations during the first day of the analysis, with values ranging between 1,800 mm and 2,600 mm. The lowest values correspond to station SCV1, which is the highest site in the network, located at 2,300 m. Intermediate values are observed at stations TDPT (1,300 m) and GRME (950 m). Conversely, the highest values are measured at stations located at lower elevations. The ZTD intensities decrease proportionally with increasing sensor elevation.
Since ZTD measures the total delay of the signal while passing through the troposphere, the trend found aligns with the hydrostatic properties of the atmosphere. A receiver placed at higher elevation experiences lower ZTD because the atmospheric column ahead the measurement point is shorter. Furthermore, since the refractive index is proportional to the content of water vapor, denser layers at lower parts of the atmosphere cause a greater ZTD.

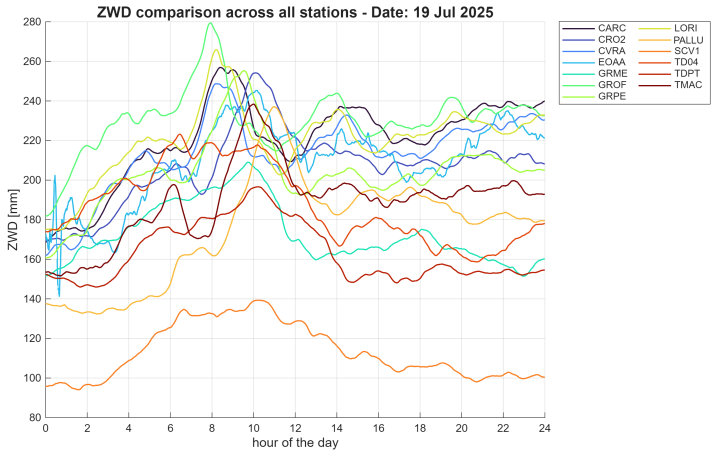

Figure 4.2: Daily time series of ZWD across the 13 GNSS stations (19 July 2025).

Zenith Wet Delay variations through the day are displayed in **Figure 4.2**. ZWD ex-

hibits a bigger temporal variability than ZTD with more pronounced fluctuations, as it depends mainly on the quantity of water vapor in the air, which is extremely variable. The mean values of the stations remain proportional to the mean values of ZTD, with higher ZWD at lower elevations and vice versa. Most stations manifest an increase in ZWD between 5 P.M. and 9 P.M., coherently with the diurnal cycle of water vapor. These peaks generally follow the high evaporation during afternoons, followed by an increased transport of water vapor.

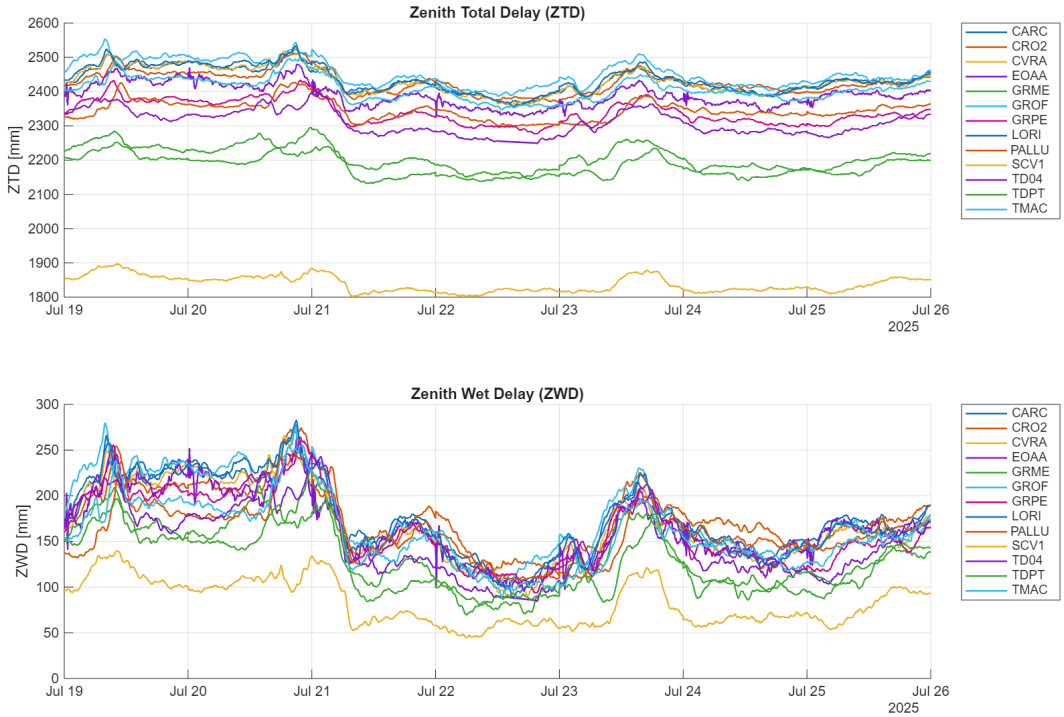

Figure 4.3: Weekly time series of ZTD (top) and ZWD (bottom) for the 13 GNSS stations.

Figure 4.3 presents the evolution of ZTD and ZWD during the observation period, from 19 July 2025 to 25 July 2025, across the 13 stations of the network. Both parameters exhibit an inverse proportionality with altitude. ZTD measurements remain within the 1,800-2,600 mm range, while ZWD oscillates between 50 mm and 300 mm. Overall, the trends in the parameters measured at different stations show a high correlation. Since they are all located in roughly the same area, they have similar meteorological characteristics.

Furthermore, the time series indicate that the first day of the analyzed period, 19 July, is characterized by a pronounced peak in ZWD values across several stations. This increase is likely associated with the presence of a moist air mass over the study area. The results highlight the good capability of Centipede low-cost stations to track rapid

temporal variations of tropospheric parameters. This performance is attributed to the high sampling frequency of 30 seconds, which helps capture fast atmospheric changes. Despite the low-cost nature of the network, the ZTD/ZWD series do not show significant outliers or instrumental noise. This demonstrates that the combination of the receivers and PPP processing provides high-quality data.

4.1.2 Elevation dependency of tropospheric delays and IWV

The dependency of ZTD on station elevation is illustrated in **Figure 4.4** (left). As expected, a strong negative correlation is observed, reflecting the reduction of the total atmospheric column at higher altitudes. The trend found is of -0.27 mm/m, meaning that for each meter of elevation there is a decrease in ZTD of 0.27 mm in the study area.
Similarly a clear relationship exists between ZWD and elevation, as shown in **Figure 4.4** (right).

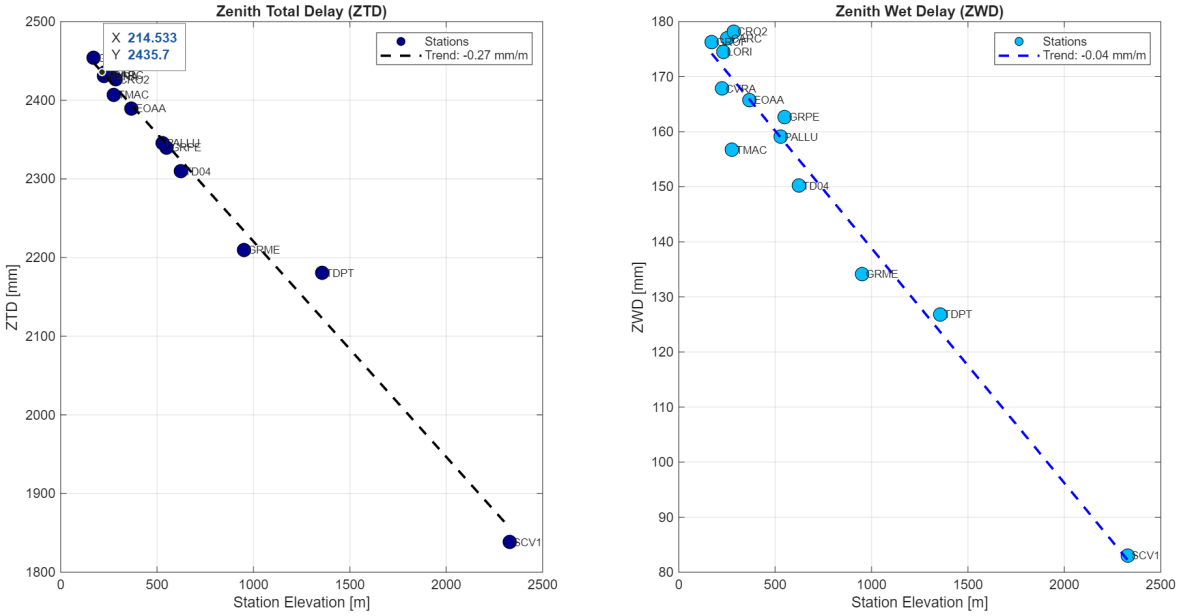

Figure 4.4: Correlation between mean ZTD (left) and ZWD (right) values and station elevation.

This trend is primarily driven by the higher concentration of water vapor in the lower layers of the troposphere; as elevation increases, the portion of the moist atmosphere above the station decreases significantly, leading to lower ZWD. The analysis reveals a vertical gradient of -0.04 mm/m.

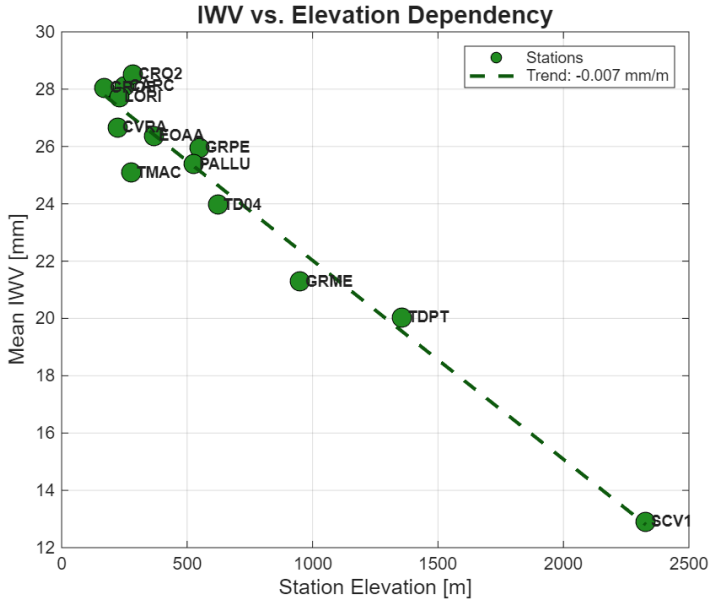

Figure 4.5: Correlation between mean IWV values and station elevation.

Furthermore, the mean IWV values were plotted against station elevation to evaluate their spatial correlation. In this case as well, the result shows an evident negative correlation, with a vertical gradient of -0.007 mm/m. This trend quantifies the IWV vertical dependency on elevation, confirming that water vapor content decreases with height across the study area.

4.2 Spatial and temporal visualization of IWV

This section illustrates the spatial and temporal evolution of Integrated Water Vapor across the study area. IWV values were derived from the ZWD measured at the 13 stations, combined with temperature values retrieved from the ERA5 reanalysis portal, applying the **Equation (3.3)** of Bevis et al. (1992).
Firstly, the results of the spatial interpolation with External Drift Kriging are presented. Then, the temporal dynamics are explored using both daily and weekly time series, as was done for tropospheric delays.
Before computing IWV, a vertical temperature correction was applied to the ERA5 dataset using the lapse rate equation **Equation (3.5)**. This adjustment is necessary because GNSS Centipede stations are rarely located at the same elevations as ERA5 grid points. The ERA5 reanalysis model operates on a global grid with a horizontal resolution of approximately 31 km $\times$ 31 km. Within each grid cell, the model assumes a uniform mean elevation distribution. Consequently, in regions characterized by mountains or valleys a significant discrepancy arises between the actual station alti-

tude and the one predicted by the model. This difference must be corrected to ensure the accuracy of the IWV retrieval.
The magnitude of this altitude gap is clearly illustrated in **Figure 4.6**. This graph highlights the residuals between the true ellipsoidal heights of the stations and the model's topographic surface. Where the difference is positive ($h_{GNSS} > h_{ERA5}$), it means that the elevation predicted by the model is lower than the actual elevation; without correction, the IWV would be overestimated meaning that the model would account for a higher atmospheric column. On the other hand, a negative difference ($h_{GNSS} < h_{ERA5}$) implies that the position of ERA5 is higher than the real position, leading to an underestimation of IWV.

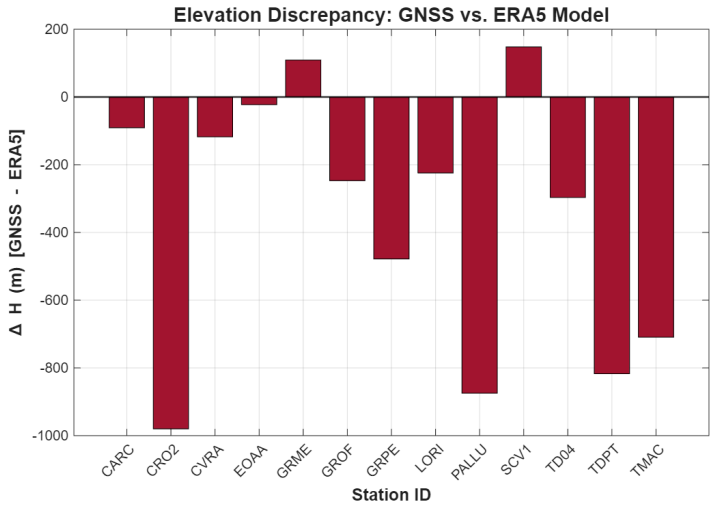

Figure 4.6: Elevation discrepancy between the GNSS stations' ellipsoidal heights and the ERA5 model orography.

By applying a vertical correction, the temperatures extracted from ERA5 are accurately adjusted to the specific height of the GNSS station, effectively eliminating these height-induced biases and ensuring the reliability of the final water vapor products.

4.2.1 IWV variogram

The characterization of the spatial variability of Integrated Water Vapor is a fundamental prerequisite for an accurate interpolation with Kriging. This process begins with the computation of the experimental semivariance, which was plotted against the lag distance to obtain the experimental semivariogram, according to **Equation (3.7)**. While the term "variogram" is frequently used in the literature for brevity, these plots are technically semivariogram.

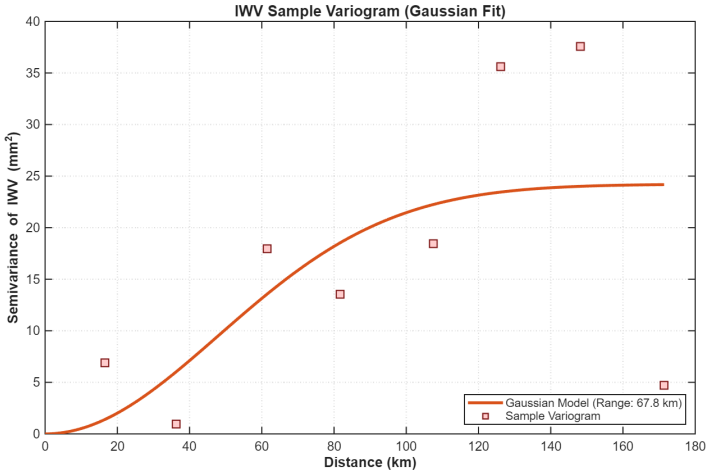

Figure 4.7: Experimental and theoretical IWV variogram. The red markers represent the binned empirical values, while the solid line indicates the fitted Gaussian theoretical model.

Figure 4.7 illustrates the experimental (or sample) variogram and the corresponding theoretical variogram. For the current study, the Gaussian model was identified as the most suitable theoretical fit for the experimental variogram. To ensure a clear and easily interpretable visualization, the experimental values were aggregated into bins. This process reduced the original 78 point pairs into 8 representative lag distances, which are the 8 red squares displayed in the graph.
The spatial distribution of IWV is characterized by a strong correlation at short distances (up to 40 km), where the low semivariance values indicate that nearby stations record consistent moisture values. This spatial correlation is formally described by a range of 67.8 km, which quantifies the maximum distance of correlation. The sill was found to be approximately 24 mm^2, which represents the maximum spatial variance between two points. Furthermore, the negligible nugget effect highlights the accuracy of IWV estimates. This result validates the low-cost network's ability to capture a reliable and smooth spatial distribution of moisture, as local-scale noise is effectively negligible.

4.2.2 IWV spatial visualization

The Integrated Water Vapor was retrieved for the entire network by integrating Zenith Wet Delay measurements with temperature data from the ERA5 dataset. Then, External Drift Kriging interpolation was implemented considering altitude as a secondary variable in the process to account for the vertical stratification of the atmosphere. This allowed for the retrieval of a homogeneous distribution of IWV values across the study area. The results include 28 maps of interpolated IWV values, 4 for each day of the

analysis. To avoid being redundant, five representative maps are discussed below. The cartographic outputs include topographic contour lines and geographic references (latitude and longitude) for the study area. The IWV magnitude is represented by a color gradient ranging from dark blue for the lowest IWV values to yellow/orange for the highest values. Intermediate IWV content is represented by greenish colors, ensuring a smooth transition across the study area. Results reveal a strong inverse correlation between IWV and elevation; lower values are always found at higher elevations, whereas in the valleys there are maximum values. A temporal trend is also observable, characterized by lower IWV values during the nights.

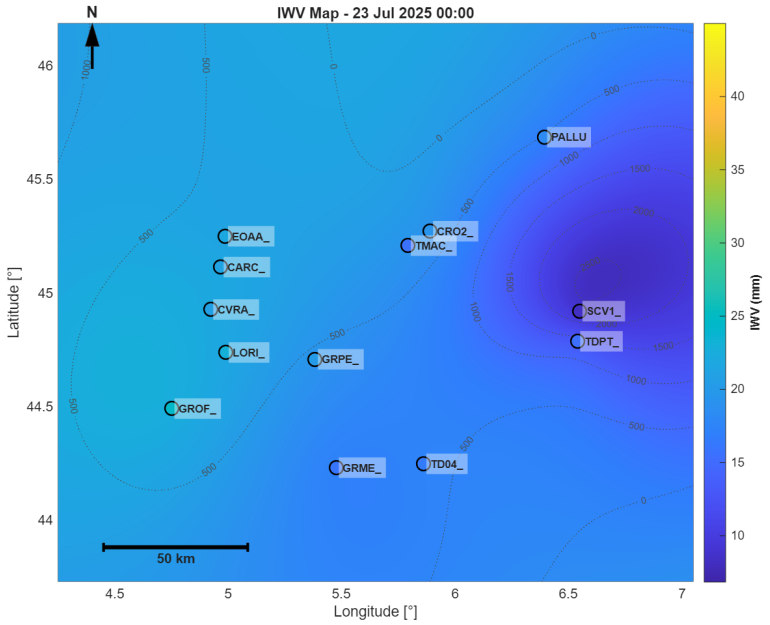

Figure 4.8: Spatial distribution of IWV on 23 July at 00:00. This map represents the driest conditions observed during the study period.

Figure 4.8 represents the driest atmospheric state recorded, which is 23 July at 00:00. In this scenario, IWV values range from 8 mm to 22 mm. IWV peaks are localized near EOAA and CARC stations, which are located respectively at 367 m and 250 m, whereas the minimum values are found at SCV1 station, near Mount Chaberton, which reaches an elevation of 3,130 m.

The highest moisture concentration was observed on 20 July at 6:00 P.M. (**Figure 4.9**), with significantly higher values varying between 17 mm and 45 mm. This great increase is justified by the rise of convective motions of water vapor during the day, typical of mid-latitude regions. This phenomenon is more pronounced in the valleys, where water vapor remains trapped within the lower layers of the atmosphere. The

spatial distribution of IWV aligns with the characteristic regional trends, as evidenced by the significantly lower values surrounding the high-altitude SCV1 station.
The EDK algorithm succeeds in capturing the steep IWV gradients and the great range of atmospheric variations. This is particularly evident in the sharp increase in IWV intensities when transitioning from the mountainous area to the TMAC, CRO2 and PALLU stations, all situated in the Isère valley.

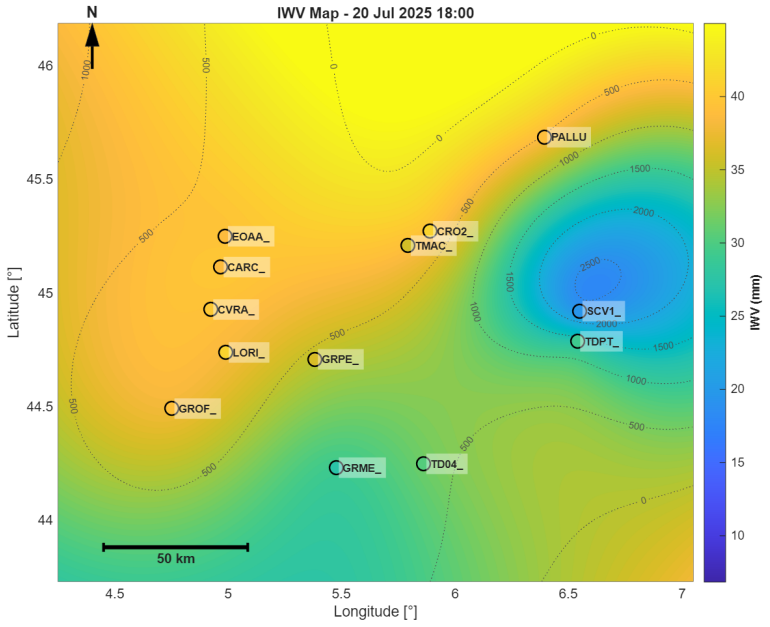

Figure 4.9: Spatial distribution of IWV on 20 July at 6:00 P.M. This map represents the most humid conditions observed during the study period.

Figure 4.10 illustrates a transitional state with intermediate IWV values, 19 July at 12:00. This moment includes IWV values that span between 19 mm and 36 mm.
The interpolation technique succeeds in assigning different IWV values to adjacent stations at different elevations, confirming the high spatial resolution of the model and its ability to capture local topographic variations. While these transitions occur smoothly across the study area, stations like TMAC, CRO2 and PALLU exhibit higher IWV magnitudes than their surrounding. As previously noted, this spatial pattern is primarily caused by their position in the Isère valley, proving that the model accurately incorporates elevation as a primary driver of water vapor distribution.

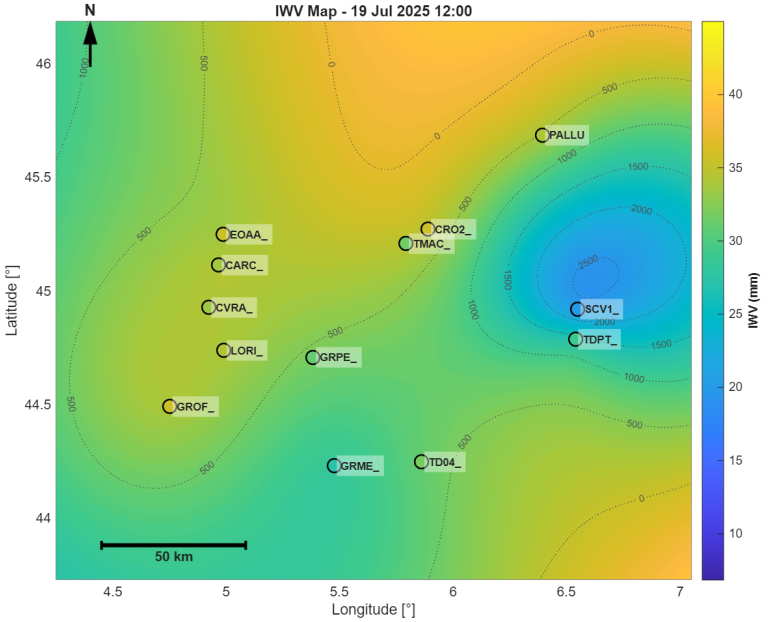

Figure 4.10: Spatial distribution of IWV during a transitional atmospheric state (19 July, 12:00). The map illustrates moderate moisture levels.

Figure 4.11 highlights the high temporal resolution of the interpolation model. Specifically, on 21 July, a rapid atmospheric transition is noticed: at 00:00, IWV reaches high values (up to 47 mm), while six hours later, at 06:00 A.M., values decrease significantly, with maximum values dropping to 38 mm. This underscores the capability of the EDK interpolation technique to report fast atmospheric changes.

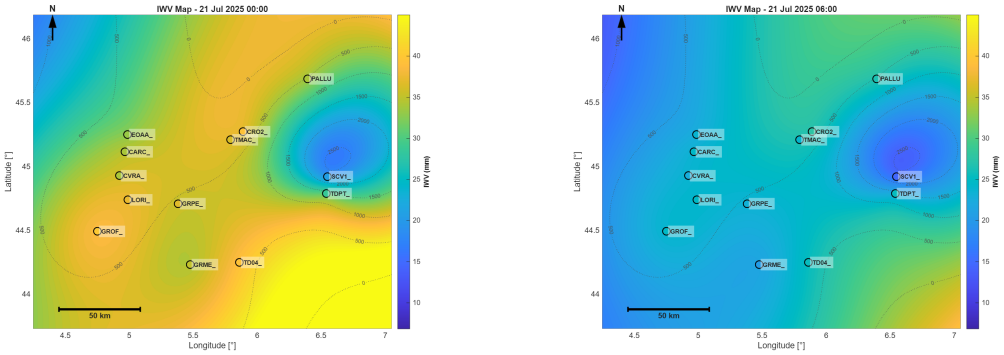

Figure 4.11: Comparison of IWV spatial distribution on 21 July at 00:00 (left) and 06:00 A.M. (right). The maps illustrate a rapid atmospheric drying event.

A comprehensive analysis of the 28 interpolation maps confirms that the spatial distribution of IWV across the study area results consistent with the regional orography.

However, the northern sector of the study area, characterized by the Parc naturel régional de Chartreuse, which reaches elevations of approximately 2,000 m, consistently exhibits overestimated IWV values. This discrepancy is attributed to a significant gap in station coverage in this specific area. The model relies on observations from TMAC, CRO2 and PALLU stations in the Isère valley to the East; and from EOAA, CARC and CVRA stations to the West, which altitudes are respectively 367 m, 250 m and 223 m. Consequently, the lack of high-altitude receivers in the northern part leads to the EDK algorithm to implement an extrapolation, causing anomalous high magnitudes of IWV.

4.2.3 IWV time series

To characterize the temporal evolution of Integrated Water Vapor across the chosen network, the time series for all 13 GNSS stations were analyzed.
Figure 4.12 displays the IWV variation through the first day of the analysis, 19 July 2025. Each colored line represents one of the 13 stations of the network, while the dashed line indicates the network mean.

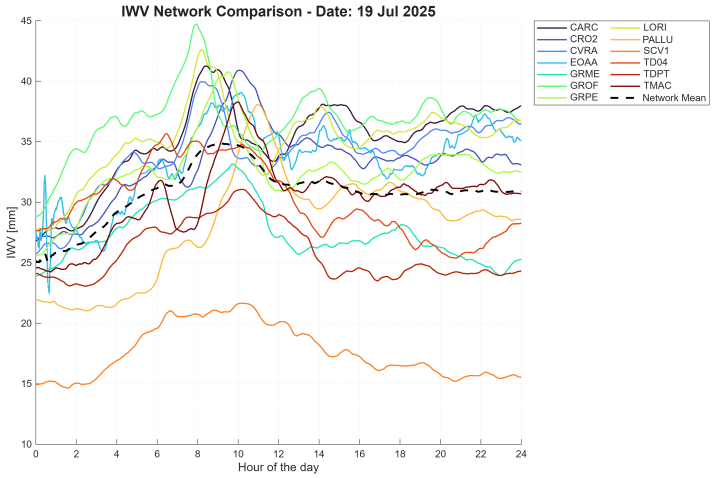

Figure 4.12: : Time series of GNSS-derived IWV for the 13 stations of the network (19 July 2025).

A clear stratification of the values is observable: the SCV1 station consistently exhibits the lowest IWV intensities, mirroring the behavior previously observed for Zenith Tropospheric Delay and Zenith Wet Delay. In contrast, high values of IWV estimates correspond to stations located at lower altitudes in the valleys.
Despite these offsets, all stations follow a synchronized trend, suggesting that a regional-scale meteorological event was driving the atmospheric moisture dynamics of the study

area. The observed temporal trend is characterized by a consistent increase between 4 and 10 A.M., followed by high-frequency oscillation for the remaining part of the day. This trend is consistently captured both by individual station time series and by the computed network mean. These high-frequency oscillations further demonstrate the network's capability to detect fast changes in IWV magnitudes.
As shown in **Figure 4.13**, the analysis was extended to the entire week. During this period, IWV values exhibit high variability, ranging from a minimum of 7 mm to peaks of 45 mm.

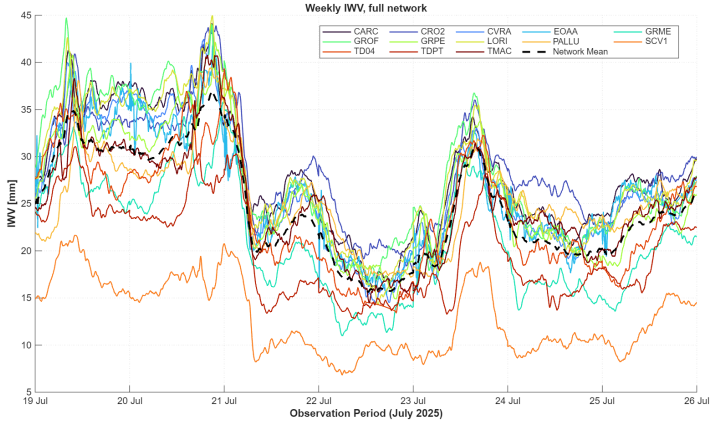

Figure 4.13: Weekly evolution of GNSS-derived IWV across the 13 stations of the network.

The weekly analysis maintains the same configuration, displaying the data for all 13 GNSS stations along with the computed network mean.
The nearly parallel trends across the 13 stations implies a good quality of the GNSS derived estimations. SCV1 remains the station with the lowest IWV values, ranging between 7 mm and 21 mm. Despite the clear offset from the other stations, SCV1 strictly follows the general trend of the network, confirming that these low values are caused by the high elevation of the station (2,328 m). This systematic offset highlights the strong vertical stratification of the atmosphere, where the reduced air column over high-altitude sites naturally leads to lower water vapor values.
Figure 4.14 illustrates the mean daily IWV trends for the analyzed period for all 13 GNSS stations. The dashed black line represents the network average. The results reinforce the previously observed correlation between altitude and water vapor content: the highest IWV values are associated with low-elevation stations characterized by higher temperatures, whereas the lowest values are found in mountain sites. As indicated by the network average, the stations follow a clear diurnal cycle, with a decrease in IWV intensities during the early morning hours and a peak in the late afternoon.

The high level of correlation in the behavior of the 13 stations confirms the accuracy of the Centipede RTK network and its capability to provide a consistent representation of the regional tropospheric dynamics.

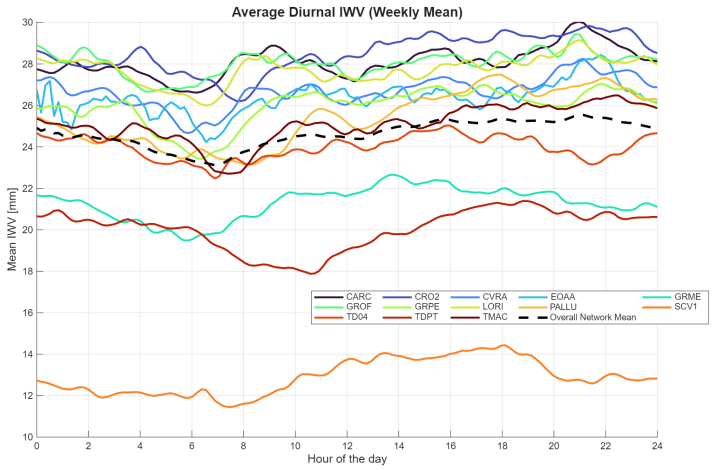

Figure 4.14: Average daily IWV profile computed over the seven-day observation period.

4.3 Validation

In this section, the performance of the interpolation model is evaluated. First, a Leave-One-Out cross-validation was performed. In this approach, each station in the network was systematically excluded from External Drift Kriging interpolation in each iteration. RMSE and bias were then computed using respectively **Equation (3.8)** and **Equation (3.9)**, by comparing the estimated value with the excluded observation.

Figure 4.15 illustrates the results for the LORI station, chosen as a representative case study due to its optimal position, as its proximity to three other network points ($\approx$ 20–30 km) ensures high spatial correlation (**Figure 3.1**).

In **Figure 4.15** the time series of IWV at station LORI are shown, comparing the observed data with the values predicted through the Leave-One-Out cross-validation procedure. The red dashed line represents the predicted IWV while the solid black line denotes the observed values. The two lines almost overlap, proving the robustness of the interpolation model and its ability to accurately reconstruct the water vapor distribution.

As indicated in the plot, RMSE and bias for the station LORI are respectively 1.15 mm and -0.60 mm. The RMSE quantifies how much the estimates deviate from the measurements. Considering the mean weekly IWV of 27.72 mm at this site, the relative error is around 4.15%. In the field of GNSS meteorology, such a low relative error is indicative of highly accurate and reliable water vapor estimates.

The bias provides an assessment of the systematic error of the model. A value of -0.60 mm indicates a slight but adequate underestimation of the IWV.

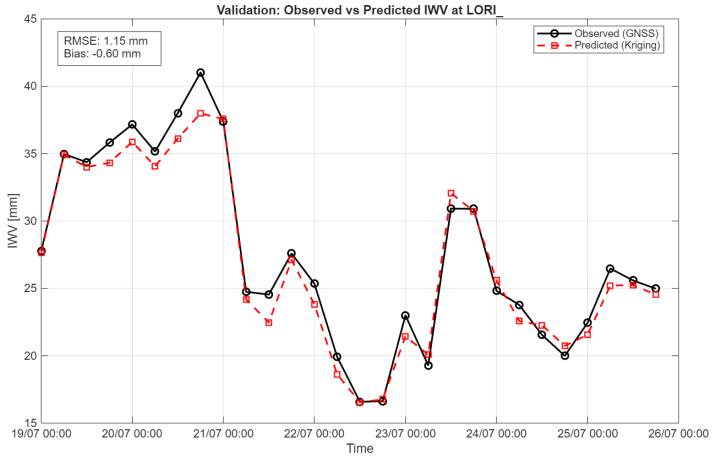

Figure 4.15: Comparison between GNSS-derived IWV (observed) and interpolated IWV (predicted) at LORI station, obtained through Leave-One-Out Cross-Validation.

The results of Leave-One-Out cross-validation for the 13-station network are summarized in **Table 4.1**.

Station ID	Ellipsoidal height [m]	Bias [mm]	RMSE [mm]
CARC	250	-0.42	0.96
CRO2	285	-1.42	1.62
CVRA	223	1.27	1.56
EOAA	367	-0.06	1.49
GRME	950	1.18	1.75
GROF	171	-0.82	1.60
GRPE	550	-0.69	1.38
LORI	230	-0.60	1.15
PALLU	527	0.33	1.75
SCV1	2329	0.32	2.89
TD04	623	0.21	1.35
TDPT	1357	-0.81	2.24
TMAC	276	0.97	1.10

Table 4.1: Results of Leave-One-out Cross-Validation: Summary of bias and RMSE for the 13 stations of the network.

Table 4.1 shows the bias and the RMSE for all 13 stations. The global mean RMSE is 1.68 mm while the global mean bias is 0.12 mm. A spatial dependency in the error distribution is evident: the highest RMSE is found at stations located at high elevations,

such as SCV1 (2,329 m, RMSE = 2.89 mm) and TDPT (1,357 m, RMSE = 2.24 mm). These high values suggest that IWV estimation remains significantly more challenging at high elevations.

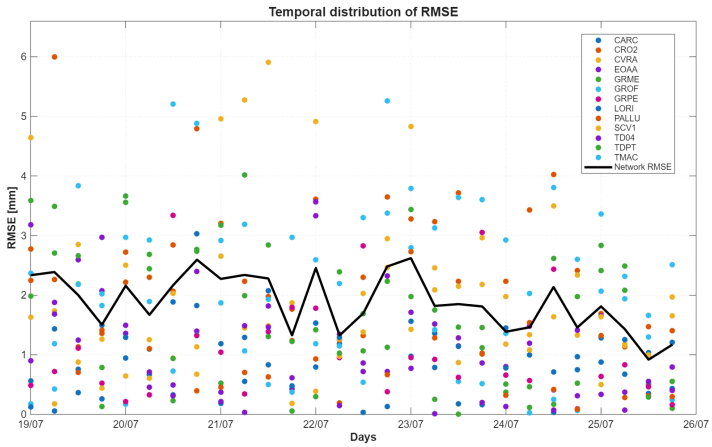

Figure 4.16: Root Mean Square Error (RMSE) results from the Leave-One-Out Cross-Validation for each GNSS station.

Figure 4.16 displays the temporal evolution of the RMSE computed with Leave-One-Out Cross-Validation for the 13 stations of the network. RMSE is computed every 6 hours. The solid black line represents the Network RMSE, computed as the average error across all 13 stations for each time step. The trend exhibits a clear cyclic variability, being influenced by daily atmospheric dynamics. The Network RMSE line oscillates between 1 mm and 2.5 mm and aligns within individual station distribution, reflecting high data coherence.

To further strengthen the reliability of the proposed model, a secondary validation approach was implemented through independent external validation. The results obtained through the 13-stations of Centipede RTK network were compared to an external reference, the BRMF station of EUREF Permanent Network at Lyon. The station was chosen because of its proximity to the original network.

The initial results of the external validation gave a RMSE of 7.90 mm, a value that exceeds the typical accuracy thresholds for GNSS-derived IWV products. This discrepancy is attributed to extrapolation errors, as the BRMF station is located outside the original 13-station network. In geostatistics, extrapolation significantly increases the uncertainty of the prediction.

To avoid this problem, an additional Centipede station was incorporated into the network, reaching a total of 14 stations (**Figure 3.2**). The addition of COMBE station, located in the northern part of Lyon, effectively integrates the BRMF station within the network boundaries. The new configuration allowed for the performance of Exter-

nal Drift Kriging and independent external validation under ideal conditions.

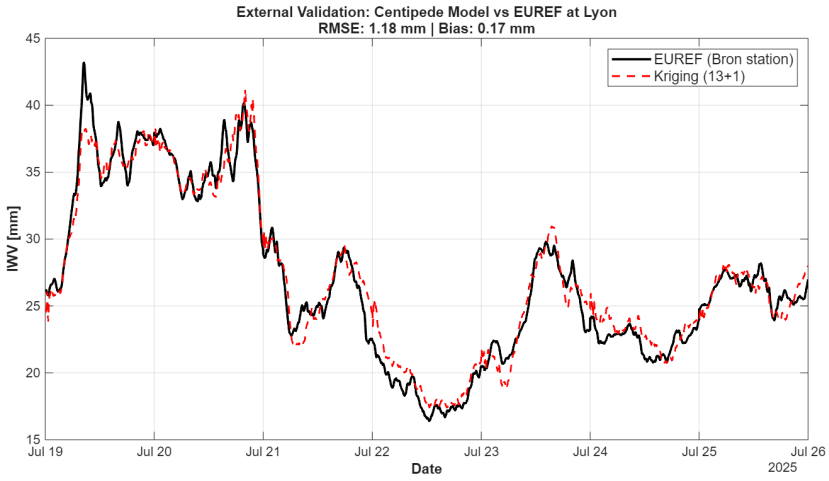

Figure 4.17: Comparison between the GNSS-derived IWV from the 14-station network (13 Centipede + COMBE) and the EUREF BRMF reference station at Lyon.

Figure 4.17 illustrates the results of the external validation conducted using the new 14-station network and the BRMF station from EUREF. By comparing the EDK-derived IWV estimates (dashed red line) and the IWV measurements at BRMF (solid black line), a significantly lower RMSE was found. The transition from extrapolation to interpolation resulted in a reduction of the RMSE to 1.18 mm, accompanied by a bias of 0.17 mm, confirming the hypothesis that the performance of the predictions is highly influenced by network geometry.

The minimal discrepancy between these datasets proves the capability of the low-cost GNSS network to predict reliable IWV estimates. Findings confirm that Centipede RTK network can achieve a predictive performance comparable to permanent networks (such as EUREF standards). This evidence supports the integration of such networks into existing meteorological infrastructures for a more detailed understanding of water vapor dynamics.

Chapter 5

Discussion

This chapter provides a comprehensive discussion of the results obtained in this analysis, placing them in the context of the existing literature. Additionally, it examines the limitations of the current study and identifies potential perspectives for future research.

5.1 Discussion of the results

While numerous studies have investigated the positioning capabilities of low-cost GNSS receivers, their application in meteorology has only gained significant attention in recent years. Current literature primarily focuses on the accuracy of Zenith Tropospheric Delay estimations, with fewer studies specifically addressing the retrieval of Integrated Water Vapor. Traditionally, IWV monitoring has been reserved for permanent geodetic networks such as the International GNSS Service (IGS) and the EUREF Permanent Network (EPN).

The present work evaluated the estimation of IWV using a 13-station network of low cost GNSS Centipede-RTK receivers, followed by spatial interpolation conducted through External Drift Kriging.

The findings of this study reveal a Network RMSE for the estimation of IWV of 1.68 mm, computed through Leave-One-Out cross-validation. This corresponds to a mean relative error of 6.8%, a value that aligns with the accuracy standards expected from low-cost GNSS infrastructures. The analysis further suggests a correlation between station elevation and RMSE magnitude, as measurement points located at higher altitudes exhibited slightly increased RMSE values.

Furthermore, the Independent External Validation against EUREF station in Lyon confirms the reliability of the estimates of IWV, yielding a RMSE of 1.18 mm.

These results are in line with recent literature focusing on IWV retrieval from low-cost GNSS networks. For instance, Bosser et al. (2024) analyzed a dataset of 265

Centipede stations and compared IWV estimates against ERA5 reanalysis data. The results show a mean bias of 0.06 kg/m^2 and a mean standard deviation of 1.48 kg/m^2. Since in meteorology 1 kg/m^2 is physically equivalent to 1 mm of precipitable water, these results are directly comparable to the ones obtained in the thesis. Although the validation in the thesis followed a slightly different approach, as the temperature was downloaded from ERA5 and subsequently transformed into IWV, the obtained RMSE remains closely aligned with the standard deviation of the paper.
Furthermore, a study by Wu et al. (2020) showed a strong correlation between IWV estimates from Centipede low-cost GNSS receivers and precipitation measurements from conventional meteorological stations.
Another significant output of this research is the demonstrated effectiveness of the External Drift Kriging in reconstructing the spatial distribution of Integrated Water Vapor. By incorporating altitude as an auxiliary variable for EDK, the model successfully captures the high-frequency spatial variations of IWV. This allows for accurate mapping even in regions with complex orography. Although the existing literature extensively discusses the use of ordinary kriging to estimate tropospheric delays, there is a lack of research applying spatial interpolation to IWV derived from low-cost GNSS stations. Furthermore, most literature relies on Ordinary Kriging, whereas the use of EDK remains significantly less explored.
For instance, Ma et al. (2020) implemented Ordinary Kriging to estimate Zenith Wet Delay using a professional Continuous Operating Reference Stations network in the Netherlands. Given the predominantly flat topography of their study area, Ordinary Kriging performed well, yielding a RMSE for ZWD between 0.7 cm and 1.2 cm. When converted to the same metric, the results obtained in this thesis are remarkably consistent with those of the paper. This is a particularly significant finding as it demonstrates that the use of EDK in topographically various regions allows low-cost receivers to achieve a level of accuracy comparable to that of standard geodetic stations, despite the latter's superior precision. Furthermore, the inter-station distances in this study, ranging from 20 to 60 km, are consistent with the typical density of the Centipede RTK network, confirming that such a spatial resolution is sufficient for effective regional tropospheric monitoring.
Additional insights can be provided by the work of Akar and Inal (2024), who conducted a comparative performance assessment of Ordinary Kriging and Inverse Distance Weighting (IDW) for spatial prediction of Zenith Total Delay. Their findings confirm that Ordinary Kriging shows a better performance than IDW, reporting a RMSE 0.92-2.95 cm in February and 1.76-3.85 cm in August. Their study relied on IGS reference with baselines between 250 km and 300 km. These extensive distances

between measurement points likely account for the higher RMSE values, contrasting with the denser station distribution employed in this thesis. The accuracy achieved in this thesis proved to be superior to the one obtained by Akar and Inal (2024), effectively proving that the high-density choice of low-cost receivers can compensate individual sensor limitations. This is particularly evident when those networks are integrated with altitude-dependent interpolation techniques.

5.2 Future perspectives

While this study successfully demonstrates the effectiveness of low-cost GNSS stations in retrieving Integrated Water Vapor and the capability of External Drift Kriging in predicting its spatial distribution, several promising directions for future development can be identified.

First, the analysis could be significantly strengthened by expanding the temporal dataset. Due to operational constraints, this research focused only on a one-week observation period. However, broadening the analysis to an entire year or more would provide a more comprehensive understanding of the seasonal variability of water vapor, allowing also for a deeper validation of the EDK model during both convective summer peaks and stable winter regimes. Extending the dataset would enhance the reliability of IWV estimates, thereby providing more robust inputs to refine and improve the accuracy of regional climate models.

Secondly, the analysis could be spatially expanded by increasing the density of the GNSS network. Incorporating a larger number of stations would significantly improve the accuracy of the spatial interpolation of the data, mitigating the risk of overestimation or underestimation of IWV in regions currently lacking station coverage. A clear example of this limitation was observed in the northern part of the study area, specifically over the Parc naturel régional de Chartreuse; here, the absence of local receivers led to overestimated IWV values, an issue that could be effectively resolved by implementing a denser network configuration.

Moreover, the GNSS data processing, currently performed through the CSRS-PPP service, could be integrated with the use of different open-source processing software such as RTKLIB. Implementing such a comparative analysis would be useful in identifying the optimal processing strategy for low-cost networks. The internal supplement of the necessary correction data by CSRS, though efficient, limits the user's control over the processing strategy. Transitioning to software that permits the independent selection of correction products would allow for a more detailed evaluation of how different processing strategies affect the final IWV accuracy.

Finally, a significant evolution of this work would be the transition from post-processing to Real-Time monitoring. This modification would make it possible to use high-density, low-cost networks like Centipede for meteorological applications. Specifically, providing continuous, high-resolution IWV maps would support current weather forecasting systems in predicting extreme meteorological events, such as intense floods or convective storms.

Chapter 6

Conclusions

This thesis evaluated the performance of the low-cost Centipede RTK network in estimating ZTD, and its consequent transformation into IWV, along with an analysis of spatial interpolation. The findings of this study are remarkable and provide a solid foundation for future development in the field of GNSS meteorology. Two primary outcomes emerge as the most significant results.

First, it was demonstrated that the analyzed network of low-cost receivers achieves an accuracy in predicting IWV that is comparable to the standards of the EUREF Permanent Network. Despite the affordable nature of the receivers, the IWV estimates proved to be highly reliable even in topographically challenging mountain regions. These findings demonstrate that individual sensor limitations do not compromise their utility for high-precision atmospheric monitoring.

Secondly, the study confirmed the high effectiveness of External Drift Kriging in reconstructing the spatial distribution of IWV. By incorporating elevation as an auxiliary variable, the model was able to model the complex vertical stratification of water vapor at varying altitudes. This analysis also highlighted the critical role of network geometry in geostatistical predictions. The independent validation against the EUREF station in Lyon initially showed a high RMSE due to extrapolation issues; however, by optimizing the network configuration with the addition of a new low-cost station, the RMSE was reduced to 1.18 mm. This shows that the predictive performance of the model is highly dependent on the spatial distribution of the stations.

These results suggest that low-cost receivers can be effectively integrated into high-grade geodetic infrastructures to address the spatial gap inherent in sparse permanent networks. The achievement of such high-resolution spatial coverage is essential for the advancement of GNSS meteorology. These networks can be used to compute water vapor used for climate models and weather forecasts. The dataset derived from these infrastructures enable a more precise characterization of the spatial and temporal dis-

tribution of water vapor, a critical parameter for improving weather prediction and climate models.

Bibliography

Akar, A. U. and Inal, C. (2024). Performance of spatial interpolation methods in predicting gnss zenith total delay. *Measurement*, 227:114227.

Bevis, M., Businger, S., Herring, T. A., Rocken, C., Anthes, R. A., and Ware, R. H. (1992). GPS Meteorology: Remote Sensing of Atmospheric Water Vapor Using the Global Positioning System. *Journal of Geophysical Research: Atmospheres*, 97(D14):15787–15801.

Bosser, P., Ancelin, J., Métois, M., Rolland, L., and Vidal, M. (2024). Evaluation of tropospheric estimates from CentipedeRTK, a collaborative network of low-cost GNSS stations. *GPS Solutions*, 28:158. Review article. Published online: 18 July 2024.

Brenot, H., Ducrocq, V., Walpersdorf, A., Champollion, C., and Caumont, O. (2006). GPS zenith delay sensitivity evaluated from high-resolution numerical weather prediction simulations of the 8–9 September 2002 flash flood over southeastern France. *Journal of Geophysical Research: Atmospheres*, 111(D15).

Bruyninx, C., Legrand, J., Fabian, A., and Pottiaux, E. (2019). Gnss metadata and data validation in the euref permanent network. *GPS Solutions*, 23:106. Accessed: 2025-11-05.

Campos, A., Munoz-Martin, J. F., Ruiz de Azua, J. A., Fernandez, L., Perez-Portero, A., Llaveria, D., Herbert, C., Pablos, M., Golkar, A., Briatore, S., Gazaniti, N., Gutierrez, A., Antonio, C., Bandeiras, J., Andrade, J., Cordeiro, D., Nichele, F., Mozzillo, R., Piumatti, A., Cardi, M., Esposito, M., Carnicero, B., Pastena, M., Filippazzo, G., and Reagan, A. (2023). Federated satellite systems/ 3 cat cubesat mission: Soil moisture and sea ice mapping using l-band microwave radiometry and gnss-r. *IEEE Geoscience and Remote Sensing Society*. L-Band frequency range analysis for soil moisture and sea ice mapping.

Centipede RTK Project (2025). Centipede-RTK: The Open and Collaborative

GNSS Network for Real-Time Kinematic Positioning. `https://centipede.fr/`. Community-based RTK correction network. Accessed: 2025-11-10.

Champollion, C., Masson, F., Van Baelen, J., Walpersdorf, A., Chéry, J., and Doerflinger, E. (2004). GPS monitoring of the tropospheric water vapor distribution and variation during the 9 September 2002 torrential precipitation episode in the Cévennes (southern France). *Journal of Geophysical Research: Atmospheres*, 109(D24).

Choy, S., Wang, C., Zhang, K., and Kuleshov, Y. (2013). GPS sensing of precipitable water vapour during the March 2010 Melbourne storm. *Advances in Space Research*, 52(9):1688–1699.

Dabove, P. and Bagheri, M. (2023). Enhancing Atmospheric Monitoring Capabilities: A Comparison of Low- and High-Cost GNSS Networks for Tropospheric Estimations. *Remote Sensing*, 15(21):5143. Article published in Remote Sensing, MDPI, 2023.

Dabove, P. and Di Pietra, V. (2024). A gnss low-cost rtk network: Positioning and atmospheric monitoring performances in mountain areas. In *Proceedings of the 2024 International Technical Meeting of The Institute of Navigation (ITM)*, pages 858–868, Long Beach, California, USA, 23-25 January.

Deutsch, C. V. and Journel, A. G. (1997). *GSLIB: Geostatistical Software Library and User's Guide*. Oxford University Press, New York, second edition.

EU Agency for the Space Programme (2025). What is gnss. Accessed: 2025-10-29.

Garrido-Carretero, M. S., de Lacy-Pérez de los Cobos, M. C., Borque-Arancón, M. J., Ruiz-Armenteros, A. M., Moreno-Guerrero, R., and Gil-Cruz, A. J. (2019). Low-cost GNSS receiver in RTK positioning under the standard ISO-17123-8: A feasible option in geomatics. *Measurement*, 137:168–178.

Global Geodetic Observing System (2025). International gnss service (igs). `https://geodesy.science/item/igs/`. Accessed: 2025-11-05.

Goovaerts, P. (1997). *Geostatistics for Natural Resources Evaluation*. Oxford University Press, New York, Oxford.

Guerova, G., Jones, J., Douša, J., Dick, G., Wilgan, K., Galane, T., Pascale, S., Demyanov, V., and Bender, M. (2016). Review of the GNSS zenith path delay estimation state-of-the-art and adjunct steps entailing the conversion to precipitable

water vapour. *Atmospheric Measurement Techniques*, 9(11):5423–5446. Comprehensive review on using permanent GNSS networks for atmospheric water vapour estimation.

Held, I. M. and Soden, B. J. (2000). Water vapor feedback and global warming. *Annual Review of Energy and the Environment*, 25(1):441–475.

Hersbach, H., Bell, B., Berrisford, P., Biavati, G., Horányi, A., Muñoz Sabater, J., Nicolas, J., Peubey, C., Radu, R., Rozum, I., Schepers, D., Simmons, A., Soci, C., Dee, D., and Thépaut, J.-N. (2023). ERA5 hourly data on single levels from 1940 to present. Accessed: 2026-02-01.

Hofmann-Wellenhof, B., Lichtenegger, H., and Wasle, E. (2008). *GNSS – Global Navigation Satellite Systems: GPS, GLONASS, Galileo, and more*. Springer.

Hohn, M. E. (1991). An introduction to applied geostatistics: by edward h. isaaks and r. mohan srivastava, 1989, oxford university press, new york, 561 p., isbn 0-19-505012-6, isbn 0-19-505013-4 (paperback), 55.00*cloth*,35.00 paper (us). *Computers Geosciences*, 17(3):471–473.

Jade, S. and Vijayan, M. S. M. (2008). GPS-based atmospheric precipitable water vapor estimation using meteorological parameters interpolated from NCEP global reanalysis data. *Journal of Geophysical Research: Atmospheres*, 113(D3):D03106.

Jin, S., Wu, X., and Qiu, H. (2021). *GNSS-Reflectometry: Fundamentals, Methods and Applications*. Springer.

Ma, H., Psychas, D., Xing, X., Zhao, Q., Verhagen, S., and Liu, X. (2021). Influence of the inhomogeneous troposphere on GNSS positioning and integer ambiguity resolution. *Advances in Space Research*, 67(6):1914–1928. Analyzes the impact of tropospheric variations on high-precision GNSS processing.

Meindl, M. (2011). *Combined Analysis of Observations from Different Global Navigation Satellite Systems*, volume 83 of *Geodätisch-geophysikalische Arbeiten in der Schweiz*. Schweizerische Geodätische Kommission (SGK), Zürich, Switzerland. Fortsetzung der Publikationsreihe «Astronomisch-geodätische Arbeiten in der Schweiz».

Mendez Astudillo, J., Lau, L., Tang, Y.-T., and Moore, T. (2018). Analysing the Zenith Tropospheric Delay estimates in on-line Precise Point Positioning (PPP) services and PPP software packages. *Sensors*, 18(2):520.

Rohm, W., Yuan, Y., Biadeglgne, B., Zhang, K., and Le Marshall, J. (2014). Ground-based GNSS ZTD/IWV estimation system for numerical weather prediction in challenging weather conditions. *Atmospheric Research*, 138:114–126.

Stępniak, K. and Paziewski, J. (2022). On the quality of tropospheric estimates from low-cost GNSS receiver data processing. *Measurement*, 199:111354.

Teunissen, P. J. G. and Montenbruck, O., editors (2017). *Springer Handbook of Global Navigation Satellite Systems*. Springer.

UN Office for Outer Space Affairs (2025). Global navigation satellite systems (gnss). Accessed: 2025-10-29.

Van Sickle, J. (2023). Differencing: Classification of GPS Positioning. Online lecture module, John A. Dutton e-Education Institute, College of Earth and Mineral Sciences, The Pennsylvania State University. Senior Lecturer; V3 Consultants, Lakewood, CO.

Wells, D., Beck, N., Delikaraoglou, D., Kleusberg, A., Krakiwsky, E. J., Lachapelle, G., Langley, R. B., Nakiboglu, M., Schwarz, K.-P., Tranquilla, J. M., and Vanicek, P. (1999). *Guide to GPS Positioning*. Department of Geodesy and Geomatics Engineering, University of New Brunswick, Fredericton, NB, Canada. Originally copyrighted by Canadian GPS Associates, 1986.

Weston, N. D. and Schwieger, V. (2014). Cost Effective GNSS Positioning Techniques. `https://www.fig.net/pub/figpub/pub49/figpub49.htm`. FIG Publication No. 49, FIG Commission 5. Accessed: 2025-11-07.

Wilgan, K., Hurter, F., Geiger, A., Rohm, W., and Bosy, J. (2017). Tropospheric refractivity and zenith path delays from least-squares collocation of meteorological and GNSS data. *Journal of Geodesy*, 91(2):117–134. Discusses spatial interpolation and refractivity modeling.

Won, J., Park, K.-D., Ha, J., and Cho, J. (2010). Effects of tropospheric mapping functions on GPS data processing. *Journal of Astronomy and Space Sciences*, 27(1):21–30.

Wu, J., Chen, Y., Bo, L., and Wu, W. (2023). Tropospheric delay retrieval using cost-effective single-frequency GNSS receivers with established reference stations. *Measurement*, 214:112760.

Wu, J., Ma, H., Wu, W., and Cheng, D. (2025). Monitoring water vapor transport in near real-time with low-cost GNSS receiver network. *Scientific Reports*, 15(1):24095.

Zuliani, D. (2021). Parte 1: Teoria sistemi GNSS. Technical report, Istituto Nazionale di Oceanografia e di Geofisica Sperimentale (OGS). Udine, 16 febbraio 2021.

Ávila Rodríguez, J. (2011). GLONASS Signal Plan. `https://gssc.esa.int/navipedia/index.php/GLONASS_Signal_Plan`. Accessed: November 2025; Navipedia article, European Space Agency.